Unveiling the orbital-selective electronic band reconstruction through the structural phase transition in $TaTe_2$

Natsuki Mitsuishi,[1,2,*] Yusuke Sugita,[2] Tomoki Akiba,[2] Yuki Takahashi,[2] Masato Sakano,[2,3] Koji Horiba,[4] Hiroshi Kumigashira,[4,5] Hidefumi Takahashi,[6,7] Shintaro Ishiwata,[6,7] Yukitoshi Motome,[2] and Kyoko Ishizaka[1,2,3,†]

[1]*RIKEN Center of Emergent Matter Science (CEMS), Wako, Saitama 351-0198, Japan*
[2]*Department of Applied Physics, The University of Tokyo, Hongo, Tokyo 113-8656, Japan*
[3]*Quantum-Phase Electronics Center (QPEC), The University of Tokyo, Hongo, Tokyo 113-8656, Japan*
[4]*Condensed Matter Research Center and Photon Factory, Institute of Materials Structure Science, High Energy Accelerator Research Organization (KEK), Tsukuba, Ibaraki 305-0801, Japan*
[5]*Institute of Multidisciplinary Research for Advanced Materials (IMRAM), Tohoku University, Sendai, Miyagi 980-8577, Japan*
[6]*Division of Materials Physics and Center for Spintronics Research Network (CSRN), Graduate School of Engineering Science, Osaka University, Toyonaka, Osaka 560-8531, Japan*
[7]*Spintronics Research Network Division, Institute for Open and Transdisciplinary Research Initiatives, Osaka University, Suita, Osaka 565-0871, Japan*

(Received 27 June 2023; revised 31 October 2023; accepted 12 December 2023; published 9 February 2024)

Tantalum ditelluride ($TaTe_2$) belongs to the family of layered transition metal dichalcogenides but exhibits a unique structural phase transition at around 170 K that accompanies the rearrangement of the Ta atomic network from a "ribbon chain" to a "butterfly-like" pattern. While multiple mechanisms including Fermi surface nesting and chemical bonding instabilities have been intensively discussed, the origin of this transition remains elusive. Here we investigate the electronic structure of single-crystalline $TaTe_2$ with a particular focus on its modifications through the phase transition, by employing core-level and angle-resolved photoemission spectroscopy combined with first-principles calculations. Temperature-dependent core-level spectroscopy demonstrates a splitting of the Ta $4f$ core-level spectra through the phase transition indicative of the Ta-dominated electronic state reconstruction. Low-energy electronic state measurements further reveal an unusual kink-like band reconstruction occurring at the Brillouin zone boundary, which cannot be explained by Fermi surface nesting or band-folding effects. On the basis of the orbital-projected band calculations, this band reconstruction is mainly attributed to the modifications of specific Ta $5d$ states, namely, the d_{XY} orbitals (the ones elongating along the ribbon chains) at the center Ta sites of the ribbon chains. The present results highlight the strong orbital-dependent electronic state reconstruction through the phase transition in this system and provide fundamental insights towards understanding complex electron-lattice-bond coupled phenomena.

DOI: 10.1103/PhysRevResearch.6.013155

I. INTRODUCTION

Layered transition metal dichalcogenides (TMDCs) MX_2 (M = transition metal, X = S, Se, Te) are quasi-two-dimensional systems that exhibit a wide variety of collective quantum phenomena [1,2]. One prime example is the charge density wave (CDW) order, which is described as a long-range periodic modulation of the electronic distribution with a concomitant lattice distortion [3–5]. Many types of CDW phases have been established in TMDCs (e.g., TaS_2 and $NbSe_2$) with their associated electronic properties such as metal-insulator transition and superconductivity [6,7]. On the other hand, the superperiodic lattice ordering (or superstructure) had also been considered from the viewpoint of molecule-like bonding of relevant orbitals [8]. Particularly in tellurides MTe_2, the importance of M-Te charge transfer and Te-Te overlap has been argued, which may make the picture of M-M and/or Te-Te local bonding more plausible as compared to sulfides and selenides [9–12]. Indeed, the CdI_2-type MTe_2 [see Figs. 1(a) and 1(d) for the undistorted trigonal $1T$ case] hosts various superperiodic patterns/clusters indicative of molecule-like bonding, such as Mo/W zigzag chains in (Mo,W)Te_2 [13], Ir dimers in $IrTe_2$ [14], and Te dimers in $AuTe_2$ [15]. Among them, group-V MTe_2 (M = V, Nb, Ta) is a common system that crystallizes in a monoclinic ($3 \times 1 \times 3$) superstructure at room temperature [Fig. 1(b); hereafter referred to as $1T''$] [16,17]. This metallic $1T''$ state is characterized by the quasi-one-dimensional M double zigzag (ribbon) chains, that might also be viewed as the superposition of linear M trimers in two directions [black dashed lines in Fig. 1(b)] [8,9]. Related to the large and anisotropic nature of lattice distortion, several unusual phenomena have been observed in VTe_2, such as the vanishment of topological surface states through the

*natsuki.mitsuishi@riken.jp
†ishizaka@ap.t.u-tokyo.ac.jp

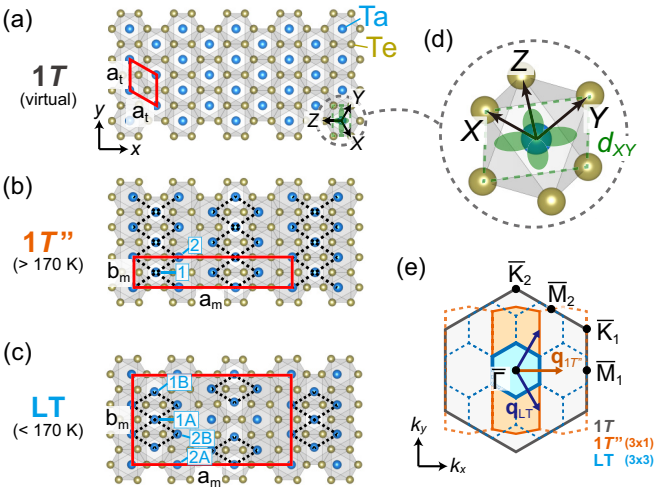

FIG. 1. Crystal structure and (001) surface Brillouin zone of $TaTe_2$. (a)–(c) Top views of $TaTe_2$ layer for the virtual undistorted $1T$ [(a), space group $P\bar{3}m1$], high-temperature $1T''$ (above 170 K) [(b), $C2/m$], and LT phases (below 170 K) [(c), $C2/m$]. The red squares indicate the (conventional) unit cells. The black broken lines in (b) and (c) highlight the characteristic Ta-Ta cluster patterns. The labels denote the inequivalent Ta sites. (d) $TaTe_6$ octahedron and the local orthogonal coordination (XYZ) adopted for the orbital-projected band calculations shown in Fig. 5. The d_{XY} orbital is depicted as an example. (e) (001) surface Brillouin zones for $1T$ (gray), $1T''$ (orange), and LT (cyan). $\mathbf{q}_{1T''}$ and $\mathbf{q}_{\mathrm{LT}}$ indicate the $\mathbf{q}$ vector of the $1T''$ (3×1) and LT (3×3) periodic lattice distortions, respectively. The crystal structures are visualized by VESTA [56].

$1T$-$1T''$ phase transition [18] and the photoinduced generation of transverse acoustic phonons [19,20]. Thus, the clustered MTe_2 compounds show a lot of promise for emerging novel electron-lattice-bond coupled phenomena.

Recently, tantalum ditelluride ($TaTe_2$) has attracted considerable interest due to its peculiar multiple patterns of Ta superstructures [21]. $TaTe_2$ is stable in the $1T''$ configuration [Fig. 1(b)] persisting up to the highest temperature, which is different from VTe_2 where the $1T$-$1T''$ phase transition occurs at a certain temperature (∼480 K) [22]. With lowering temperature, $TaTe_2$ undergoes a first-order structural phase transition at $T_s \sim 170$ K from ($3 \times 1 \times 3$) $1T''$ to a ($3 \times 3 \times 3$) low-temperature (LT) phase [Fig. 1(c), $C2/m$]. This transition is accompanied by a substantial displacement of some Ta atoms along the $\mathbf{b}_m$ axis (up to ∼0.28 Å), resulting in the formation of the "butterfly-like" Ta clusters [21,23]. We note that this LT structure is unique to $TaTe_2$ and has not been observed in other TMDCs including its sister compounds such as TaX_2 (X = S, Se) or MTe_2 (M = V, Nb). At T_s, the electrical resistivity (magnetic susceptibility) shows an abrupt drop (increase) upon cooling [21] whereas the Seebeck coefficient indicates a sign inversion [24], thereby suggesting the modifications of the electronic band structure. Recent investigations have shown that the $1T''$-LT phase transition can be controlled by various approaches such as chemical substitution [24–27], pressure application [28], photodoping [29], reduced dimensionality [30,31], and some of them also induce superconductivity [25,26,28]. Nevertheless, the underlying mechanism of the $1T''$-LT transition is still controversial, and multiple scenarios have been proposed in terms of Fermi surface nesting [27,32], anisotropic electron-phonon coupling [21,27], and local chemical bonding [24,33–36]. Since comparable Ta $5d$ and Te $5p$ states are theoretically predicted to reside near the Fermi level [10,11,21,29,34], resolving the orbital-specific modifications in the electronic states through the $1T''$-LT transition may provide important clues to fully discuss this complex phase transition and related physical properties.

In this paper, we investigate the electronic structure of single-crystalline $TaTe_2$ and its modifications through the $1T''$-LT transition by utilizing core-level and angle-resolved photoemission spectroscopy (core-level PES and ARPES) with first-principles calculations. Our temperature-dependent measurements reveal a sizable splitting of the Ta $4f$ core-level PES spectra and an unusual kink-like band reconstruction at the Brillouin zone boundary, demonstrating the significant orbital-dependent electronic state modifications in this system.

II. METHODS

Single-crystalline $TaTe_2$ were grown by the chemical vapor transport method using iodine as a transport agent. A stoichiometric mixture of Ta and Te powders and iodine was sealed in evacuated quartz tubes and reacted for about 1 week in a three-zone furnace. The temperatures of the source and growth zones were set to 900 and 800 °C, respectively. Several single crystals without multiple in-plane domains were selected by screening with polarized light microscopy and low-energy electron diffraction (LEED) measurements. Details regarding the sample characterizations, including the electrical resistivity, Seebeck coefficient, and LEED measurements, are provided in Appendix A.

Core-level PES measurements were performed at BL28A in Photon Factory (KEK) using a system equipped with a Scienta Omicron SES2002/DA30 electron analyzer. The photon energy and energy resolution were set to 90 eV and 30 meV, respectively. High-resolution ARPES measurements were conducted at the Department of Applied Physics, The University of Tokyo, equipped with a VUV5000 He-discharge lamp and a Scienta Omicron DA30 electron analyzer. The photon energy ($h\nu$) and energy resolution were set to 21.2 eV (He Iα) and 16 meV, respectively. For all measurements, the samples were cleaved *in situ* at around room temperature to obtain a fresh (001) plane and the vacuum level was kept better than 2×10^{-10} Torr throughout the measurements. The Fermi level of the samples was referenced from the Fermi-edge spectra of polycrystalline gold electrically in contact with the samples. For the ARPES data analysis, we used an empirically obtained work function of 4.9 eV.

The electronic band structures were calculated by using the OPENMX code [37]. For the virtual $1T$ phase, we adopted the local density approximation with the Perdew-Zunger parametrization for the exchange-correlation functional in the density functional theory [38] and an $8 \times 8 \times 8$ $\mathbf{k}$-point mesh for the calculations of the self-consistent electron density and the structural optimization. We optimized the lattice structure of the virtual $1T$ phase by relaxing the primitive translational vectors and atomic positions in a nonrelativistic calculation with the convergence criterion less than 0.01 eV/Å about the interatomic forces. The optimized lattice constants were

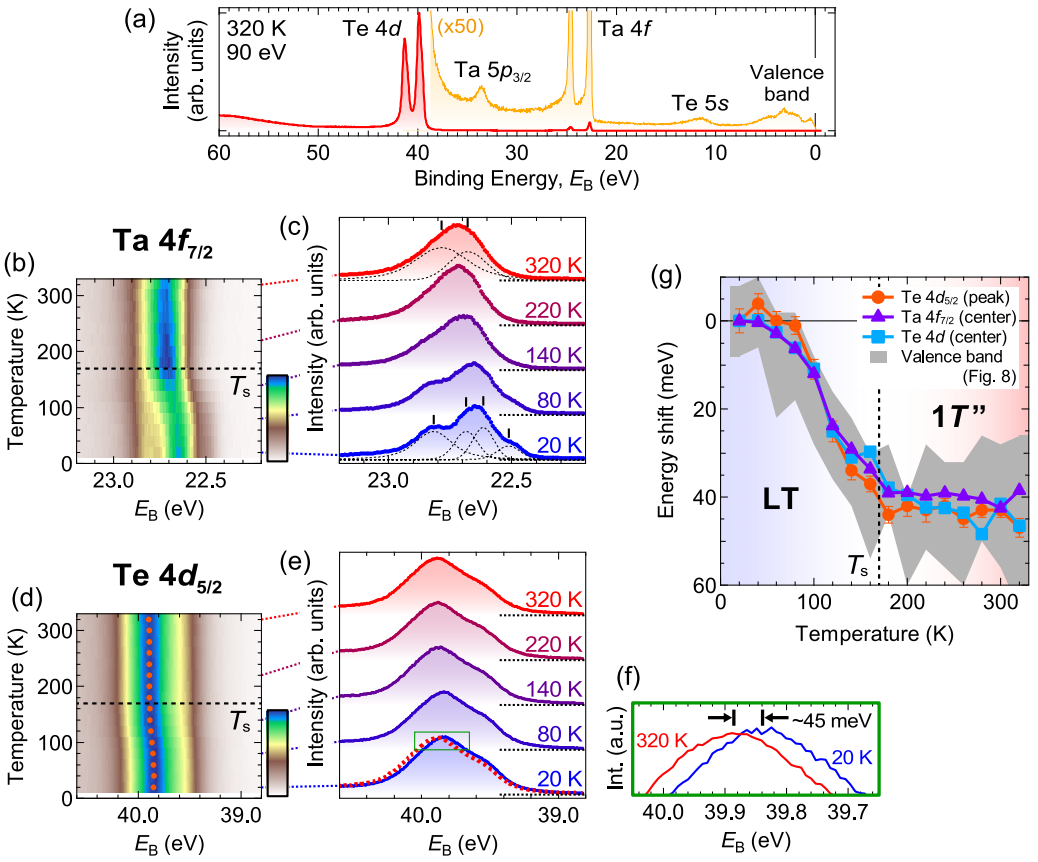

FIG. 2. Temperature dependence of core-level spectra. (a) Overall core-level photoemission spectra measured at 320 K. The magnified profile (×50, orange) is also shown for clarity. (b), (c) Temperature-dependent evolution of the Ta $4f_{7/2}$ core-level intensity color map [(b)] and spectral profiles at selected temperatures [(c)]. The black dotted curves in (c) indicate the fitting Voigt functions at 320 and 20 K (see also Appendix B). (d), (e) Same as (b) and (c), but for the Te $4d_{5/2}$ core level. The orange circle markers in (d) trace the highest intensity peak positions. The spectrum at 320 K (the broken red curve) is also overlaid on the data at 20 K for comparison in (e). (f) Close-up comparison of the peak top of Te $4d_{5/2}$ spectra [the green rectangle in (e)] at 320 and 20 K. (g) Temperature dependence of energy position shifts (relative to the values at 20 K) for the highest intensity peak of Te $4d_{5/2}$ (orange circles), the center of spectral weight of Ta $4f_{7/2}$ (purple triangles), and Te $4d$ (including $4d_{5/2}$ and $4d_{3/2}$, cyan rectangles). The gray shaded region shows the possible energy shift estimated from the temperature-dependent valence band measurements (see Appendix C). All the data in this figure were collected with a synchrotron light source ($h\nu = 90$ eV).

$a_t = 3.636$ Å and $c_t = 6.674$ Å. Using the optimized structures, we calculated the electronic band structures by a relativistic *ab initio* calculation, where the relativistic effects are included by a fully relativistic j-dependent pseudopotential. For the $1T''$ and LT phases, we calculated the electronic band structures by the generalized gradient approximation (GGA) using the experimentally reported structural parameters in the literature [21]. We adopted the Perdew-Burke-Ernzerhof GGA (PBE-GGA) functional in density functional theory [39], an $8 \times 8 \times 8$ **k**-point mesh, and a fully relativistic j-dependent pseudopotential for the calculations of the self-consistent electron density. For direct comparison with ARPES data, we constructed the proper spectral weights by employing the unfolding procedure [40,41] based on the primitive (virtual) $1T$ unit cell.

III. RESULTS

A. Core-level spectra

First, we demonstrate the temperature dependence of the core-level PES spectra that provides direct insight into the atomic site-specific electronic modulations. Figure 2(a) presents the overall core-level spectra in the high-temperature $1T''$ phase (320 K) collected using a synchrotron light source ($h\nu = 90$ eV). The intense Ta $4f$ and Te $4d$ doublet peaks are discerned at binding energies (E_B) of 22–25 and 39–42 eV, respectively, together with other core levels (see the magnified profile depicted in orange). Figures 2(b) and 2(c) show the temperature dependence of the Ta $4f_{7/2}$ core-level intensity demonstrated as the color map and the set of spectral profiles, respectively. They are collected in the temperature range from 320 to 20 K during the cooling process. The spectral profile of Ta $4f_{7/2}$ above T_s (~170 K) is broad and asymmetric with its peak position nearly fixed at $E_B \sim 22.7$ eV. Upon lowering the temperature below T_s, the peak position gradually shifts toward lower E_B and a multipeak structure emerges. This temperature-dependent splitting is reproduced in the temperature cycle and by bulk-sensitive soft x-ray measurements (see Appendix B), thereby substantiating its bulk origin. To quantify the splitting energies, we performed a fitting analysis using two/four Voigt functions with a Sherly-type background for the $1T''$/LT phase, respectively, by considering the

numbers and types of inequivalent Ta sites [see Figs. 1(b) and 1(c)]. The analysis yields the maximum splitting energies of 0.11(3) and 0.31(3) eV for $1T''$ (320 K) and LT (20 K), respectively, as displayed by the black markers and dotted curves in Fig. 2(c) (see Appendix B for more details). This implies that the variation of the electron densities among the inequivalent Ta sites (i.e., d-d charge transfer) is substantially enhanced across the transition. Meanwhile, we note that these splitting energies are much smaller as compared to those in the Star-of-David CDW systems such as $1T$-TaS_2 (∼1.2 eV) [42] and $1T$-$TaSe_2$ (∼0.9 eV) [43], where strong electron-electron correlation effects (Mott transition) often intertwine with the $\sqrt{13} \times \sqrt{13}$ superperiodic states [6,44,45].

Similarly, the temperature dependence of the Te $4d_{5/2}$ core level is extracted as shown in Figs. 2(d) and 2(e). Since there are three inequivalent Te sites in $1T''$, the spectra above T_s already feature a multipeak structure. In contrast to Ta $4f_{7/2}$, the Te $4d_{5/2}$ spectral distribution hardly changes even below T_s. This indicates that the charge redistribution among the Te sites (p-p charge transfer) across the transition is negligible compared to that of the Ta sites. On the other hand, we find a slight shift of the peak maximum toward a lower E_B at lower temperatures as indicated by the orange circle markers in Fig. 2(d). This is more clearly seen in the overlaid profiles at 320 K (red) and 20 K (blue) in Figs. 2(e) and 2(f), where the peak positions differ by about 45 meV. To examine this shift more precisely, we compare the temperature dependence of the energy shift (relative to the value at 20 K) estimated by the position of the highest intensity peak for Te $4d_{5/2}$ (orange circles) and the center of the spectral weight for Ta $4f_{7/2}$ (purple triangles) and Te $4d$ (including both $4d_{5/2}$ and $4d_{3/2}$, cyan rectangles), as displayed in Fig. 2(g). Remarkably, both the Ta $4f$ and Te $4d$ shifts show nearly the same temperature dependence, indicating that the amount of the Ta-Te charge transfer (d-p charge transfer) is not significantly modified upon the $1T''$-LT transition. We attribute this uniform shift mainly to the temperature-dependent chemical potential shift, which is also consistent with the temperature-dependent variation of the valence band position as highlighted by the gray shaded area (see Appendix C for this estimation). This behavior is in stark contrast to another $5d$ system $IrTe_2$, where the trigonal-triclinic transition at ∼280 K is accompanied by the Ir dimerization and significant d-p charge transfer, resulting in the core-level PES splitting of both Ir $4f$ and Te $4d$ [46]. The present results of core-level PES on $TaTe_2$ thus suggest that the Ta state is strongly modified whereas the Te state remains mostly intact through the $1T''$-LT phase transition.

B. Electronic band structure

Next, we focus on the valence band structure. For simplicity, we use a set of high-symmetry points based on the primitive (virtual) $1T$ unit cell [see Fig. 1(e) for the (001) surface Brillouin zone (BZ)]. Here we define $\bar{K}_1/\bar{K}_2$ and $\bar{M}_1/\bar{M}_2$ points that become inequivalent in the $1T''$ phase as compared to virtual $1T$. Figure 3(a) shows the two-dimensional curvature plot [47] of the ARPES intensity map at the Fermi level (E_F) recorded in the high-temperature $1T''$ phase (300 K), obtained by using a He-discharge lamp ($h\nu$ = 21.2 eV). The original ARPES intensity plots are provided in Appendix D. We find the signature of multiple warped Fermi surfaces extending along the $\bar{\Gamma}-\bar{M}_1$ (k_x) direction, which is perpendicular to the Ta ribbon chains in the real space (i.e., the $\mathbf{b}_m$ axis). We note that such highly anisotropic Fermi surfaces are successfully observed because of the well-separated single domain. In the case of multidomain samples, the signal mixing from multiple in-plane 120° domains should be carefully considered [18,48,49]. Figure 3(b) displays the curvature plots of the ARPES spectra recorded along the $\bar{\Gamma}-\bar{K}_{1(2)}-\bar{M}_{1(2)}-\bar{\Gamma}$ lines. Of particular interest relevant to the quasi-one-dimensional Fermi surface are the bands residing at the virtual $1T$ BZ boundaries. There are several dispersive bands that cross E_F along $\bar{M}_1-\bar{K}_1$. In contrast, two relatively flat bands lie at $E_B \sim 0.6$ and 0.9 eV along $\bar{M}_2-\bar{K}_2$. These characteristic bands, together with the quasi-one-dimensional Fermi surfaces, are very similar to those observed in the isostructural $1T''$-VTe_2 [18] and are also qualitatively well reproduced within our band-unfolding calculation ($k_z = 0$) as shown in Figs. 3(c) and 3(d).

In Figs. 3(e)–3(h), we present the results for the LT phase in a similar manner as in Figs. 3(a)–3(d). The experimental data shown in Figs. 3(e) and 3(f) are collected at 15 K. While at first glance the Fermi surface contour in Fig. 3(e) is almost unchanged from $1T''$ [Fig. 3(a)], we observe a substantial spectral reconstruction in the band dispersion [Fig. 3(f)]. Along $\bar{\Gamma}-\bar{K}_2$ and $\bar{\Gamma}-\bar{M}_2$, the hole-like bands split into sharp submanifolds with small energy gaps (typically 50–150 meV), as denoted by the red arrows. These features are well reproduced by our band calculation as shown in Fig. 3(h). While most of the spectral weight is concentrated on the original $1T''$ bands, a closer comparison between ARPES and calculation (Appendix E) can also trace the additional faint band structures that are distributed with the LT (3×3) periodicity. Thus, we attribute these modifications essentially to the band-folding effect [40]. On the other hand, at around $\bar{M}_1$ (the BZ boundary), a linear band dispersion gets strongly modified as marked by the white arrow in Fig. 3(f), which is difficult to explain by the simple band-folding effect (will be discussed later).

To further inspect the band modifications across the transition, we systematically compare the original ARPES intensity plots near E_F along several momentum cuts covering the $1T$ BZ, as shown in Figs. 4(a) and 4(b). The positions of the momentum cuts (#1-#7) are depicted on the Fermi surface map in Fig. 4(c). Here, the data at 300 K [Fig. 4(a)] are divided by the Fermi-Dirac distribution function convoluted with the Gaussian resolution function to remove the thermal smearing effect of the Fermi-Dirac cutoff. The cyan curves and blue circle markers in Figs. 4(a) and 4(b) indicate the momentum distribution curves at E_F and their peak positions (i.e., Fermi momentum) given as a guide to the eye, respectively. We find several types of modifications upon cooling, such as band segmentation predominantly seen in cuts #1 and #2, and the upward shift of the E_F-crossing Λ-shaped band as depicted by the white dotted lines in cuts #3 and #4. These changes can be well explained by the band-folding effect and chemical potential shift described above, respectively. Rather, the most striking change is found in the intense V-shaped inner band around the BZ boundary (cuts #6 and #7), centered at $k_y = 0$. In cut #7 (i.e., $\bar{K}_1-\bar{M}_1-\bar{K}_1$), these "inner" V-shaped bands

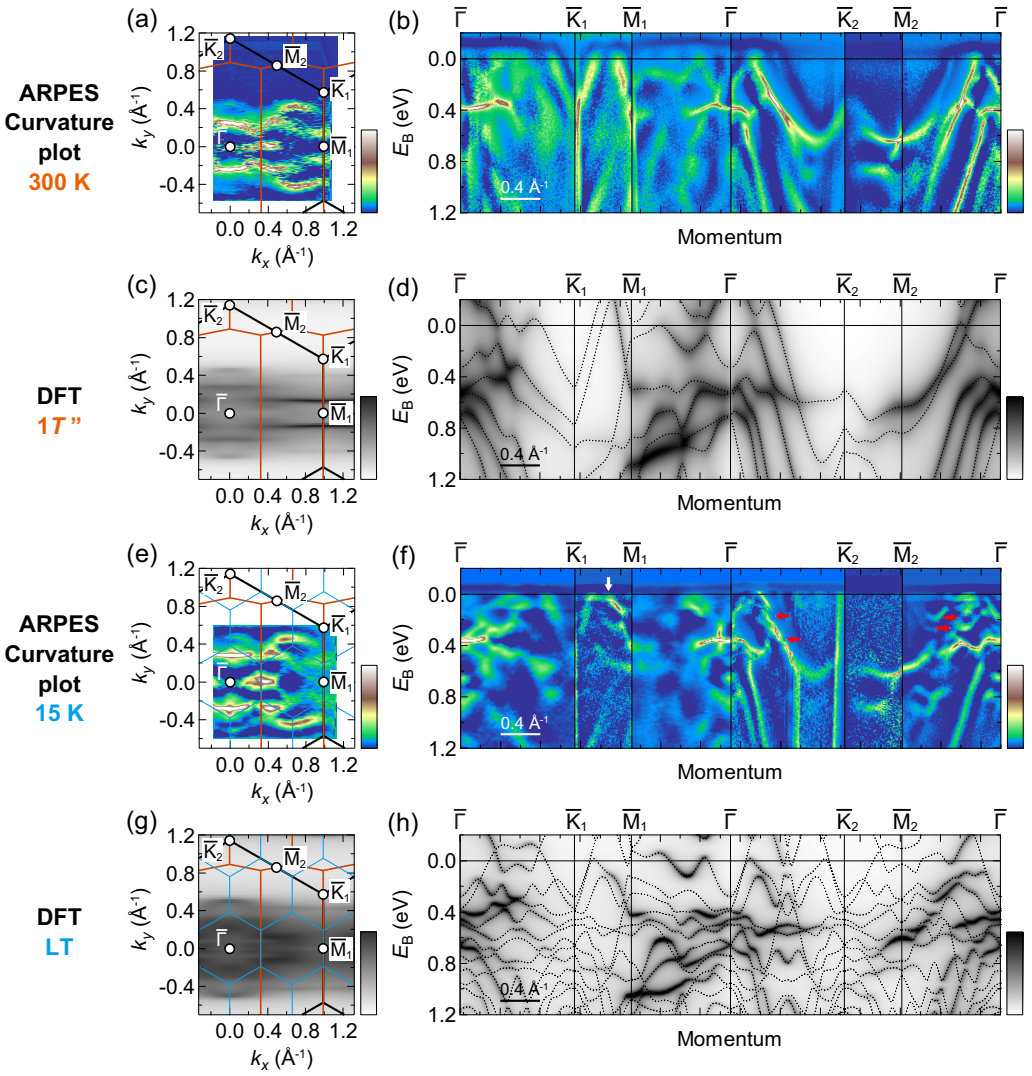

FIG. 3. Overview of electronic band structure. (a) Two-dimensional curvature plot of the ARPES intensity map at E_F (integral width: 20 meV) in the $1T''$ phase (300 K) collected with a He-discharge lamp ($h\nu = 21.2$ eV). The regular and elongated hexagons indicate the (001) surface Brillouin zones of virtual $1T$ and $1T''$, respectively. (b) Curvature plot of the ARPES spectra at 300 K along $\bar{\Gamma}-\bar{K}_{1(2)}-\bar{M}_{1(2)}-\bar{\Gamma}$. Note that the color scale bars of the curvature plots are shown inverted (i.e., while-brown colors mean negative values). The original ARPES intensity plots are provided in Appendix D. (c), (d) Band-unfolding calculation for the $1T''$ phase ($k_z = 0$) of the Fermi surface [(c)] and band dispersions [(d)]. The whole band dispersion is presented by dashed lines in (d). (e)–(h) Same as (a)–(d), but for the LT phase (ARPES data: 15 K). The cyan hexagon indicates the (001) surface Brillouin zone of LT. The red arrows mark the characteristic spectral segmentation features. The white arrow highlights the conspicuous band modification appearing around $\bar{M}_1$.

transform into a pair of less-dispersive kink-like structures with about 70% decreased gradient, and their near-E_F spectral intensity becomes abruptly suppressed at an end point momenta $k_1\prime$. Indeed, as displayed in Fig. 4(d), the energy distribution curve at $k_1\prime$ exhibits a characteristic peak at $E_B \sim 70$ meV (the triangle marker), which is absent in that at the Fermi momenta (k_1) in 300 K. Again, this band reconstruction goes beyond the simple band-folding effect. This is in line with a recently reported temperature-dependent optical conductivity spectrum [50], where the sudden decrease in the Drude width (i.e., scattering rate) is observed upon cooling across T_s, together with the appearance of a sharp peak at 800 cm^{-1} indicative of some interband transition. This energy (∼100 meV) is close to that of the strong band reconstruction observed in the present ARPES (∼70 meV), as depicted by the triangle markers in Figs. 4(b) and 4(d).

Here we remark on Fermi surface nesting, which has been discussed in some recent works [27,32] as the possible driving force of the $1T''$-LT transition. In our ARPES results, while it is difficult to fully capture the Fermi surface topology due to the complex band structures even for $1T''$, we still readily identify a set of warped Fermi surfaces around $|k_y| \sim 0.4$ Å^{-1}, as their Fermi momentum highlighted by the blue filled markers in Figs. 4(a) and 4(c). This "outer" Fermi surface is also observed in the LT phase [Fig. 4(b)] with a slight increase in $|k_y|$ seemingly due to the chemical potential shift. To examine its temperature dependence, we show in Fig. 4(d) the energy distribution curves at the Fermi momentum in cuts

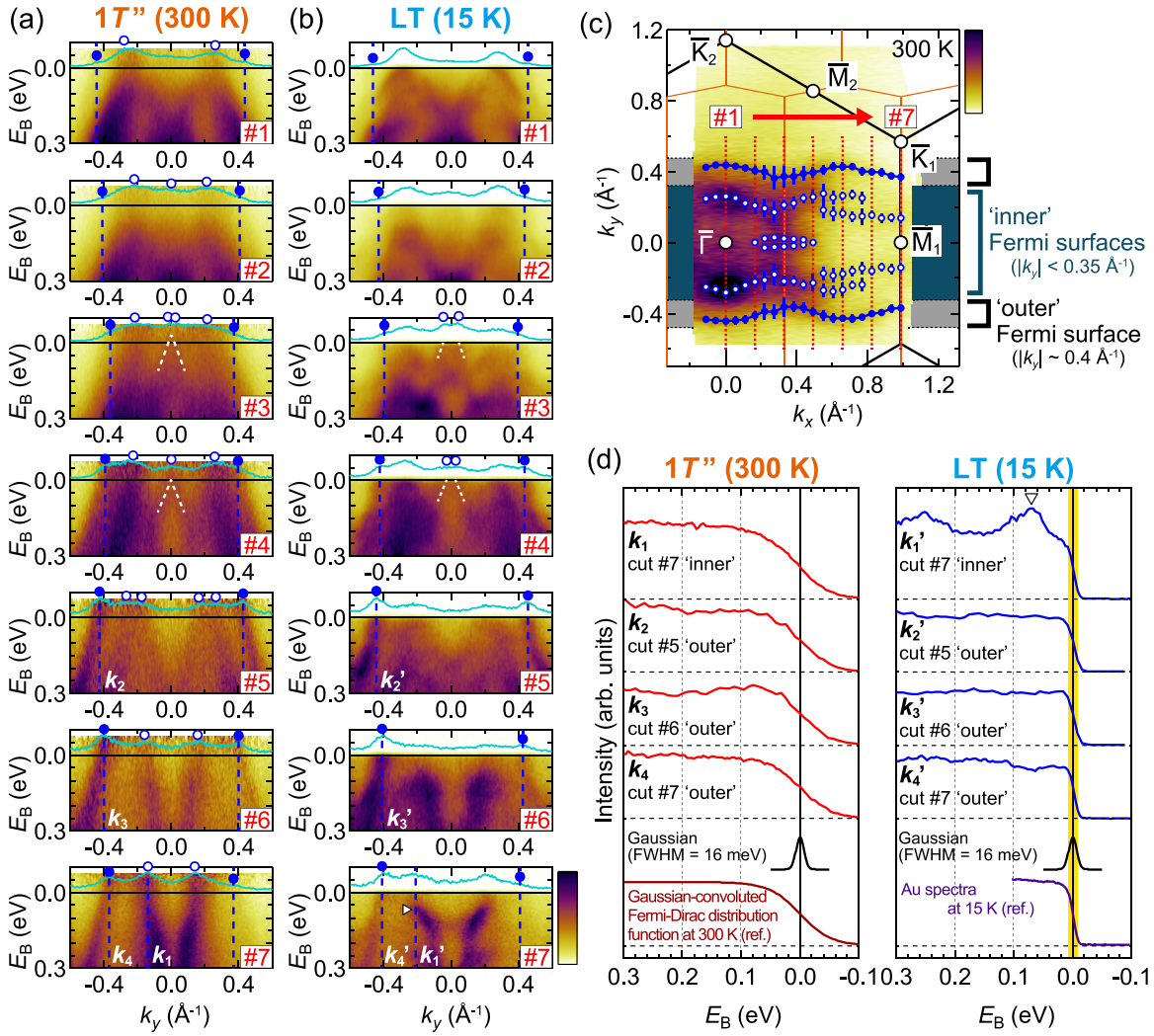

FIG. 4. Temperature dependence of Fermi-level crossing bands. (a), (b) ARPES spectra along selected momentums [cuts #1–#7, shown in (c)] for the $1T''$ (300 K) (a) and LT (15 K) phases (b). The data of (a) is divided by the Fermi-Dirac distribution function to visualize the band structure near E_F. The cyan curves show the momentum distribution curves at E_F (integral width: 20 meV). The blue filled circles (at $|k_y| \sim 0.4$ Å^{-1}) trace the "outer" Fermi surface, whereas the open circles (in $|k_y| < 0.35$ Å^{-1}) partly track the complex "inner" Fermi surfaces, displayed as a guide to the eye. The white broken lines in cuts #3 and #4 indicate the Λ-shaped band that forms the small Fermi pocket. The triangle marker in cut #7 at 15 K [(b)] depicts the location of the abrupt intensity suppression of the V-shaped band. (c) ARPES intensity map at E_F at 300 K overlaid with the peak plots extracted from the momentum distribution curves at E_F. (d) Energy distribution curves (integral width: 0.05 Å^{-1}) at selected momentums shown in (a) and (b) ($k_1 - k_4$ and $k_1\prime - k_4\prime$). The energy-resolution Gaussian (FWHM of 16 meV), the simulated Gaussian-convoluted Fermi-Dirac distribution function at 300 K, and the Au spectra collected at 15 K are also shown for reference.

#5–#7 (labeled as $k_2 - k_4$ and $k_2\prime - k_4\prime$ for 300 and 15 K, respectively), where the "outer" bands are clearly resolved. For all spectra in both phases, the spectral weight in the vicinity of E_F obeys the Gaussian-convoluted Fermi-Dirac distribution function, similar to the numerical simulation for 300 K and the experimental Au spectra at 15 K shown in the bottom of Fig. 4(d). This indicates that the outer Fermi surface is retained without any gap formation at E_F through the transition and is thus irrelevant to the Fermi surface nesting. Regarding the "inner" bands (located in $|k_y| < 0.35$ Å^{-1}) including the V-shaped band at $\bar{M}_1$, they are strongly modified at LT. Compared to the **q**-vector size of the LT (3×3) periodic lattice distortion [$|\mathbf{q}_{LT}| \sim 0.67$ Å^{-1}; see Fig. 1(e)], however, the length of the momentum vector connecting these inner bands along the $\mathbf{q}_{LT}$ direction is far short (at most ~0.4 Å^{-1}). Therefore, our results do not support the simple Fermi surface nesting scenario as the origin of the $1T''$-LT transition.

C. Orbital character

Now we discuss the band orbital character. We introduce the regular octahedral coordination with orthogonal *XYZ* axes [see Fig. 1(d)], where the distortions in the actual $TaTe_6$ octahedrons are omitted. This is a very simple but helpful model for capturing the band properties at the BZ boundary in the trigonal $1T$-type TMDCs, based on the concept of the "hidden Fermi surface" raised by Whangbo *et al.* [8,51]. Here, the three equivalent t_{2g} *d* orbitals ($d_{XY}/d_{YZ}/d_{ZX}$)

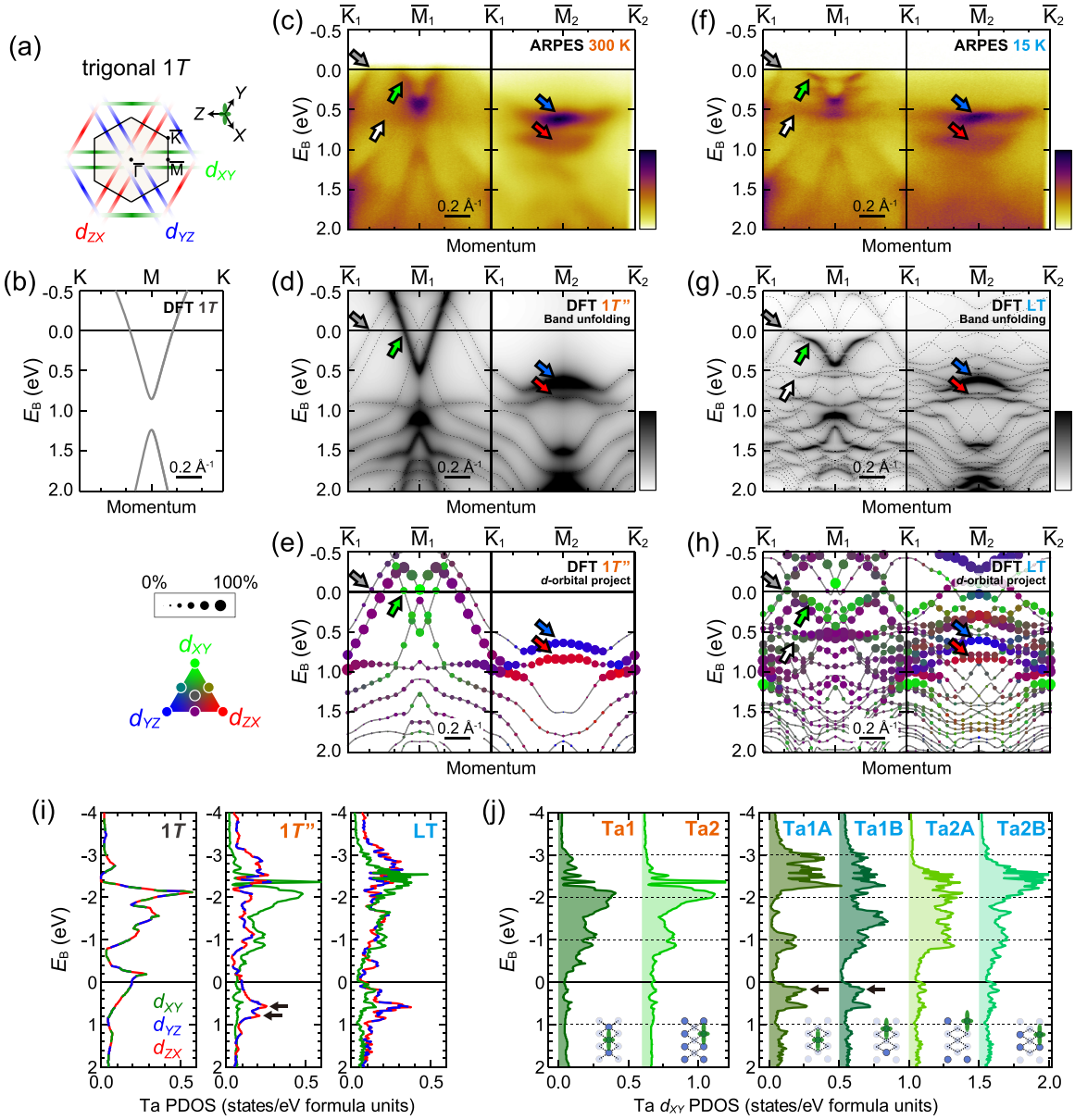

FIG. 5. Orbital-dependent band reconstructions. (a) Basic concept of the hidden Fermi surface proposed in the trigonal 1T-MX_2. The three independent t_{2g} ($d_{XY}/d_{YZ}/d_{ZX}$) σ bonds form the Fermi surface around the Brillouin zone boundary. (b) Calculated band dispersion along $K-M-K$ for the virtual 1T-$TaTe_2$. (c)–(e) ARPES data [300 K, (c)], band calculation with its unfolding spectra [(d)], and Ta t_{2g} orbital-projected band calculation [(e)] along $\bar{K}_1-\bar{M}_1-\bar{K}_1$ and $\bar{K}_1-\bar{M}_2-\bar{K}_2$ for the 1T'' phase. (f)–(h) Same as (c)–(e), but for the LT phase (ARPES data: 15 K). The green and blue/red arrows mark the d_{XY}-dominated V-shaped band and the $d_{YZ/ZX}$-dominated flat bands, respectively, whereas the gray arrow indicates the Te p-derived E_F-crossing band that forms the "outer" Fermi surface. The white arrow depicts the band dispersion peculiar to the LT phase but its remnant is still observed in the ARPES spectra at 300 K [(c)]. (i) Calculated PDOS of the Ta site-averaged $d_{XY}/d_{YZ}/d_{ZX}$ for the virtual 1T, 1T'', and LT phases. The arrows mark the d_{YZ}/d_{ZX} PDOS peaks in 1T'' corresponding to the flat bands around $\bar{M}_2$. (j) Calculated PDOS of the Ta site-resolved d_{XY} for the 1T'' and LT phases. The arrows indicate the d_{YZ}/d_{ZX} PDOS peaks in Ta1A/Ta1B sites (LT) that partly reflect the kink-like band structures appearing around $\bar{M}_1$.

respectively form one-dimensional σ-bonding states along the edge-sharing octahedral network, and their combination can constitute the hypothetical Fermi surface as illustrated in Fig. 5(a). Since the σ bonding is parallel to $K-M-K$, the resulting band structure exhibits a dispersive V shape along this direction [see Fig. 5(b) for the virtual 1T-$TaTe_2$]. Though the hybridization with the chalcogen p orbitals should be carefully considered for each case [11], this concept has been essentially demonstrated by first-principles calculations for various metallic 1T-type TMDCs [18,52,53].

The above concept can be further extended to discuss the band characters in the present 1T'' and LT phases of $TaTe_2$, as shown in Figs. 5(c)–5(e) and 5(f)–5(h), respectively. Figures 5(c)–5(e) respectively show the ARPES image, band calculations with their unfolding spectra, and Ta 5d orbital-projected band calculations along $\bar{K}_1-\bar{M}_1-\bar{K}_1$ and

$\bar{K}_1-\bar{M}_2-\bar{K}_2$, obtained for the $1T''$ phase. The size and color of the markers in Fig. 5(e) represent the total amount of the t_{2g} d-orbital contribution and the ratio of the $XY/YZ/ZX$ component, respectively, at each eigenstate (each orbital projection is presented in Appendix F). As described above, the strongly anisotropic quasi-one-dimensional band structures are realized in $1T''$, i.e., the E_F-crossing V-shaped band at $\bar{M}_1$ and the two flat bands at $\bar{M}_2$, as marked by the green and red/blue arrows in Fig. 5(c), respectively. These bands are well reproduced by our calculations [Figs. 5(d) and 5(e)] and are mainly derived from the Ta d_{XY} and d_{YZ}/d_{ZX} orbitals, respectively (note that the Z axis is perpendicular to the Ta chain direction, the $\mathbf{b}_m$ axis). It can also be recognized in the calculated partial density of states (PDOS) distributions in Fig. 5(i). Under the (hypothetical) trigonal $1T$ phase, the $d_{XY}/d_{YZ}/d_{ZX}$ orbitals are equivalent as shown in the left panel of Fig. 5(i). As for the twofold monoclinic $1T''$ [the middle panel in Fig. 5(i)], in contrast, the d_{YZ}/d_{ZX} (the blue/red curves) shows the sharp peaks at $E_B \sim 0.6$ and 0.8 eV corresponding to the flat bands, whereas the d_{XY} (the green curve) is rather featureless in this energy region. We note that a similar electronic structure has been already demonstrated in the sister compound (V,Ti)Te_2, where the formation of the d_{YZ}/d_{ZX} flat bands upon cooling are observed at $E_B \sim 0.2$ eV around the $\bar{M}_2$ point [18]. There, the flat bands were discussed in terms of the localized electronic state formed by the molecular-like trimerized vanadium bonding.

Figures 5(f)–5(h) show the band dispersions for the LT phase, in a similar manner as Figs. 5(c)–5(e). Although the original calculated band structure for LT [the thin curves in Fig. 5(h)] contains so many branches due to the folding, its unfolded image [Fig. 5(g)] is directly comparable to the ARPES data [Fig. 5(f)] and the $1T''$ results [Figs. 5(c) and 5(d)]. Both the ARPES spectra and the calculations indicate that the d_{YZ}/d_{ZX}-dominated flat bands at $\bar{M}_2$ are scarcely modified through the $1T''$-LT transition, whereas the d_{XY}-derived V-shaped band at $\bar{M}_1$ exhibits a substantial reconstruction into unusual kink-like structures. We note that the present PBE-GGA band calculations do not explicitly include the many-body interactions with low-energy elementary excitations such as phonon and polaron, thus ruling out their dominant contribution to the kink-like structures. To discuss this modification, we present in Fig. 5(j) the Ta site-specific PDOS calculations for d_{XY} in the $1T''$ and LT phases (the full set of Ta PDOS data are provided in Appendix F). While the PDOS for Ta1/Ta2 in $1T''$ and Ta2A/Ta2B in LT [see Figs. 1(b) and 1(c) for the site notations] exhibit the broad shape with no significant structures below E_F, those for Ta1A/Ta1B in LT exhibit the multiple peak structures in a wide E_B region. The peak just below E_F (black arrows) partly reflects the end point of the kink-like band structure observed in $\bar{K}_1-\bar{M}_1-\bar{K}_1$ [the green arrows in Figs. 5(f)–5(h)]. Hence, we suggest that the d_{XY} orbital states of Ta1A/Ta1B are predominantly modified through the $1T''$-LT transition.

We add notes on the orbital character of the "outer" Fermi surface discussed in Fig. 4. The band calculation in $1T''$ [Figs. 5(d) and 5(e)] reproduces the outer band near $\bar{K}_1$ as marked by the gray arrow. The corresponding marker sizes as displayed in Fig. 5(e) are fairly small, indicating its Te $5p$-dominated nature. The band calculations for the LT phase [Figs. 5(g) and 5(h)] show that this "outer" band remains crossing E_F with similar dispersion relation, which agrees well with the experimental observations. This robustness of the Te $5p$-derived state through the transition is also consistent with the temperature-independent Te $4d$ core-level PES spectra presented in Figs. 2(d) and 2(e).

IV. DISCUSSION AND CONCLUSION

The present findings can be summarized as follows: (i) The core-level PES showed the temperature-dependent splitting of the Ta $4f_{7/2}$ core-level spectra through the transition (up to ~0.31 eV) in stark contrast to Te $4d_{5/2}$, suggesting the electronic reconstruction occurring predominantly on Ta sites. (ii) The temperature-dependent ARPES measurements (from 300 to 15 K) revealed notable modifications including the sizable chemical potential shift (~45 meV), additional (3×3) folding of band dispersions, and the unusual kink-like band reconstruction ($E_B \sim 70$ meV) occurring around the BZ boundary ($\bar{M}_1$ point) in the LT phase. (iii) Comparison with the orbital-projected band calculations indicated that the kink-like band reconstruction primarily originated from modifications in the d_{XY} orbital states at the center Ta sites of the zigzag ribbons (i.e., Ta1 and Ta1A/Ta1B), whereas the d_{YZ}/d_{ZX}-derived flat bands (around $\bar{M}_2$) and the Te $5p$-dominated "outer" Fermi surfaces remained relatively

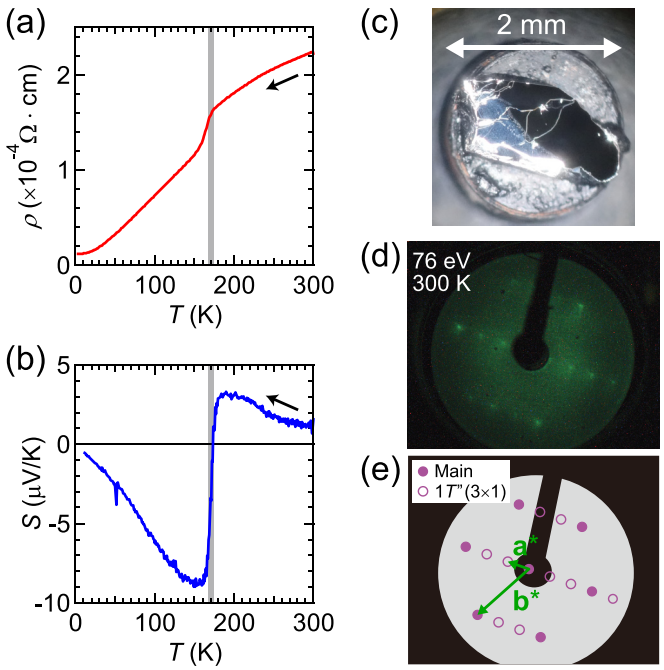

FIG. 6. Sample characterization. (a), (b) Temperature dependence of the electric resistivity [(a)] and the Seebeck coefficient [(b)] measured in the cooling cycle. Both show anomalies at around 170 K. The residual resistivity ratio ($\rho_{300\,K}/\rho_{2\,K}$) is ~18. (c) Optical microscope image of $TaTe_2$ single crystal after cleavage. (d) Low-energy electron diffraction (LEED) image collected at 300 K (electron beam energy: 76 eV). (e) Sketch of the LEED spots in (d). The filled (open) makers depict the primitive (superlattice) diffraction spots. $\mathbf{a}^*$ and $\mathbf{b}^*$ indicate the primitive reciprocal lattice vectors in $1T''$, where $|\mathbf{a}^*|$ is equal to $|\mathbf{b}^*|/3$.

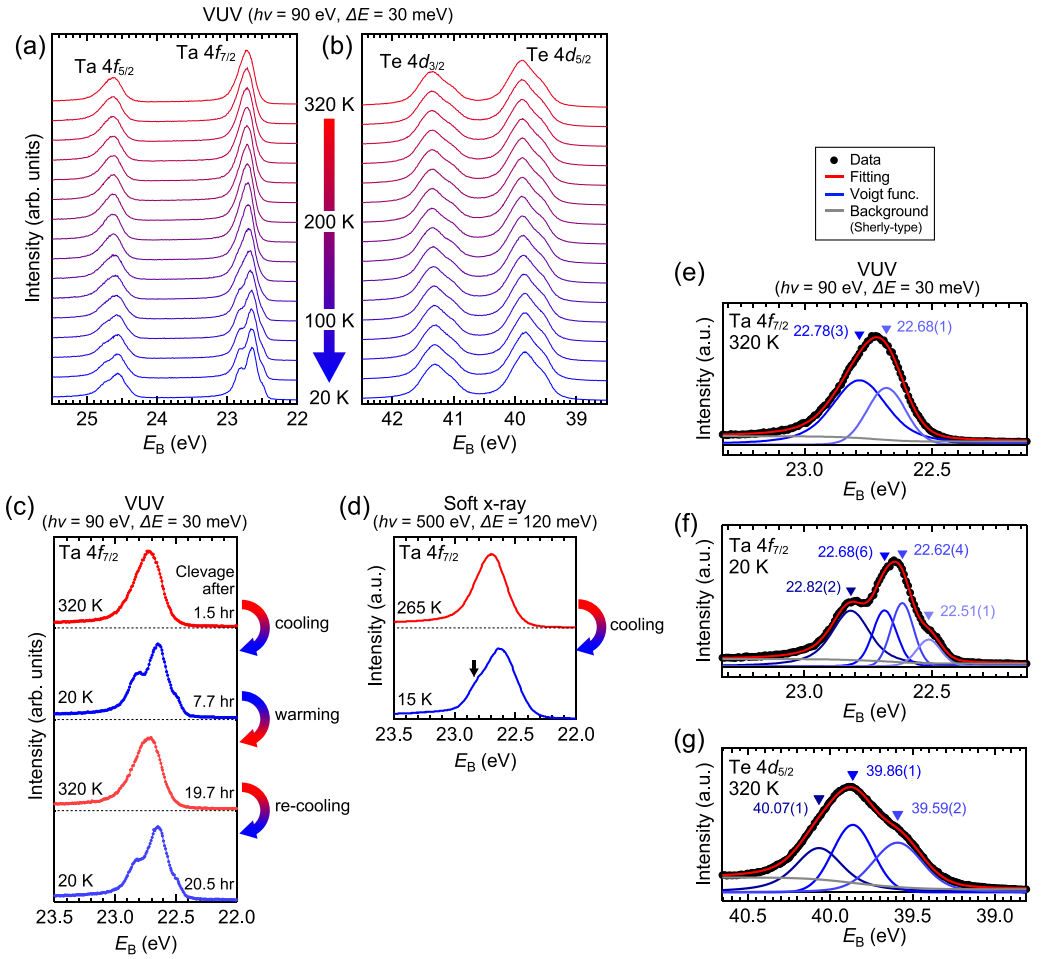

FIG. 7. Overall profiles, reproducibility of the Ta $4f_{7/2}$ splitting, and fitting analysis. (a), (b) Temperature-dependent core-level spectra of Ta $4f$ (both $4f_{7/2}$ and $4f_{5/2}$) [(a)] and Te $4d$ ($4d_{5/2}$ and $4d_{3/2}$) [(b)] collected with VUV photons ($h\nu = 90$ eV, $\Delta E = 30$ meV). (c) Temperature-cycle measurements of Ta $4f_{7/2}$ between 320 and 20 K. The elapsed time after the sample cleavage is also denoted. (d) Soft x-ray measurements of the Ta $4f_{7/2}$ spectra at 265 and 15 K ($h\nu = 500$ eV, $\Delta E = 120$ meV). The arrow marks a hump structure appearing in the LT phase. (e), (f) Fitting analysis of the Ta $4f_{7/2}$ core-level profile at 320 K [(e)] and 20 K [(f)] by using two/four Voigt functions with a Sherly-type background. (g) Fitting result of the Te $4d_{5/2}$ profile at 320 K with three Voigt functions.

unaffected throughout the transition. These results highlight the strong orbital-selective electronic modifications in this material. Our results also rule out a simple Fermi surface nesting scenario as the origin of the $1T''$-LT phase transition and may instead suggest some additional chemical bonding involving the Ta1 (Ta1A/Ta1B) sites. Indeed, recent x-ray diffraction studies [36,54] imply the possible role of Ta-Ta chemical bonding that induces the instability of the Ta1 position. However, the mechanism that drives the transformation from the ribbon chain to the butterfly-type Ta patterns needs to be further investigated, e.g., by using the out-of-equilibrium ultrafast experiments.

Finally, we would like to discuss the inherent structural fluctuation emerging above T_s, which is relevant to the present ARPES results. According to the work by Sörgel *et al.* [21], the room-temperature $TaTe_2$ hosts an anomalously large atomic displacement parameter of Ta1 atoms along the $\mathbf{b}_m$ axis (i.e., $U_{22} \sim 0.04$ Å^2, which exceeds more than twice the values of U_{11} and U_{33}). This indicates that the ribbon chain pattern in $TaTe_2$ has some prominent instability towards additional distortion, appearing as the strong fluctuation of the Ta1 atomic positions. We also point out that an unusual convex-upward electrical resistivity curve [21,24,27,28,34,50,55] as well as a broad Drude component in the optical conductivity spectrum (about 20 times broader from 300 to 5 K) [50] are also reported above T_s, suggesting that the electrons are strongly scattered in this regime. In this respect, our ARPES data at 300 K [Fig. 5(c)] already exhibits a faint kink-like feature near E_F (marked by the green arrow), together with an unusually blurred spectral weight lying at $E_B \sim 0.5$ eV between $\bar{M}_1$ and $\bar{K}_1$ (marked by the white arrow). Although anomalously broad, these features are rather characteristic of the LT phase [Figs. 5(f)–5(h)] and are completely lacking in the $1T''$ calculation [Figs. 5(d) and 5(e)] under static atomic configurations (a more detailed data analysis is provided in Appendix G). This indicates that the strong Ta1 atomic fluctuation indeed affects the electronic band structure, giving rise to the anomalous electronic properties. In this viewpoint, a comprehensive structure analysis on the bulk group-V MTe_2 (M = V, Nb, Ta) would be informative to elucidate whether such structural fluctuation is ubiquitous in $1T''$-type MTe_2 compounds [16,17,54].

In conclusion, we systematically investigated the electronic structure of $TaTe_2$ through the $1T''$-LT structural phase transition by using core-level PES, ARPES, and first-principles calculations. The present results reveal the strong orbital dependence of electronic state modifications through the $1T''$-LT transition, as demonstrated by the Ta $4f$ core-level splitting and the kink-like band reconstruction at the BZ boundary. Our findings provide important keys towards understanding the complex electron-lattice-bond coupled phenomena emerging in various metallic systems.

ACKNOWLEDGMENTS

The authors acknowledge Naoyuki Katayama for valuable discussions and Satoshi Yoshida, Bruno Kenichi Saika, Ryu Yukawa, and Miho Kitamura for soft x-ray PES measurements. N.M. and Y.S. acknowledge the support by the Program for Leading Graduate Schools of the University of Tokyo, Advanced Leading Graduate Course for Photon Science (ALPS) and Material Education program for the future leaders in Research, Industry and Technology (MERIT), respectively. Y.S. acknowledges the support by Japan Society for the Promotion of Science through a research fellowship for young scientists. Parts of the numerical calculations were performed in the supercomputing systems in ISSP, the University of Tokyo. The experiments were partly performed under KEK-PF proposals (No. 2018G093 and No. 2018G624). This work was partly supported by the JSPS KAKENHI (Grants No. JP19H05825, No. JP19H05826, No. JP20H01834, No. JP21H01030, No. JP21H05235, and No. JP22H00107).

APPENDIX A: SAMPLE CHARACTERIZATION

Figures 6(a) and 6(b) respectively show the temperature dependence of electrical resistivity and Seebeck coefficient measured in our single-crystal $TaTe_2$ sample. Both exhibit significant anomalies around 170 K, indicating the $1T''$-LT structural phase transition. Figure 6(c) displays a typical optical microscope image of our sample after cleavage. We found no signature of the mixing of in-plane 120 ° domains in our sample by polarization microscope measurement. The homogeneity of our sample is also verified by LEED measurement as shown in Fig. 6(d). As schematically depicted in Fig. 6(e), all observed diffraction spots at 300 K can be attributed to either the main Bragg peaks (filled markers) or the $1T''$ (3×1) superlattice peaks aligning along one direction (open markers).

APPENDIX B: DETAILS OF CORE-LEVEL SPECTRA

1. Overall profiles

Figures 7(a) and 7(b) display the temperature-dependent core-level spectra of Ta $4f$ (including $4f_{7/2}$ and $4f_{5/2}$) and Te $4d$ ($4d_{5/2}$ and $4d_{3/2}$), respectively, collected during the cooling process with a vacuum-ultraviolet (VUV) light source ($h\nu = 90$ eV, energy resolution $\Delta E = 30$ meV). The data shown in Figs. 2(b)–2(f) are identical to these data. We find that the Ta $4f_{5/2}$ (Te $4d_{3/2}$) spectra show a similar temperature dependence as the Ta $4f_{7/2}$ (Te $4d_{5/2}$) ones.

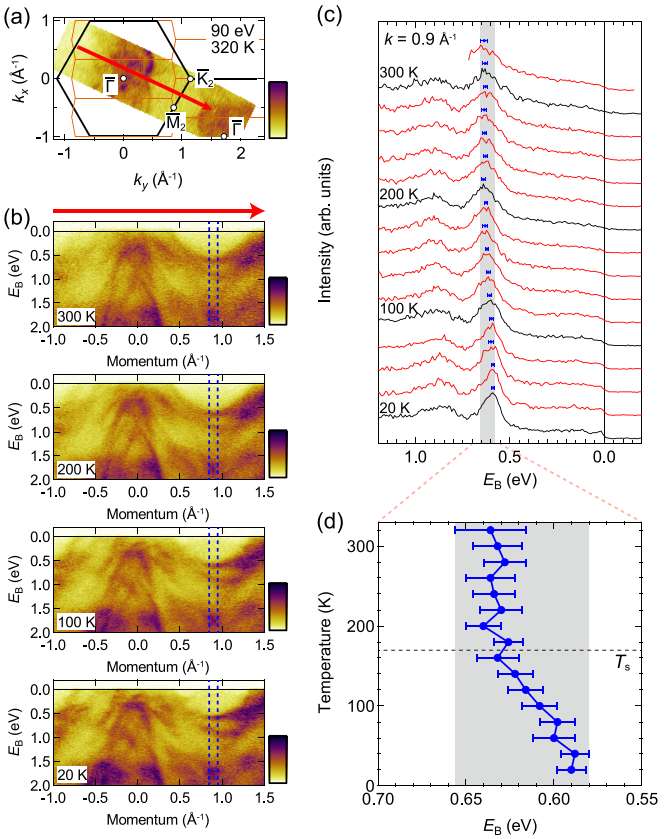

FIG. 8. Temperature dependence of the energy position of the flat band. (a) ARPES intensity plot at Fermi level collected at 320 K ($h\nu = 90$ eV). The red arrow indicates the momentum cut shown in (b). (b) The temperature-dependent ARPES spectra at selected temperatures. (c) Energy distribution curves at a momentum of ~0.9 Å^{-1} (integral width: 0.1 Å^{-1}), collected from 320 to 20 K at intervals of 20 K. The blue markers with error bars show the peak positions of the upper flat band lying at $E_B \sim 0.6 - 0.65$ eV. The gray shading is a guide for the eyes. (d) Extracted plot of the flat band position from (c).

2. Reproducibility of the Ta $4f_{7/2}$ splitting

Figure 7(c) shows the temperature-cycle measurement of the Ta $4f_{7/2}$ profiles taken at 320 and 20 K (the elapsed time after the sample cleavage is also denoted). We confirm that the splitting is reproducible and hence intrinsic to the LT phase. Furthermore, we performed bulk-sensitive measurements by employing a soft x-ray light source ($h\nu = 500$ eV, $\Delta E = 120$ meV). The soft x-ray measurements were conducted at BL2A (MUSASHI) in Photon Factory (KEK). As depicted in Fig. 7(d), a distinct hump structure emerges at $E_B \sim 22.8$ eV upon cooling from 265 to 15 K as indicated by the arrow. This feature corresponds to the splitting observed in the VUV measurement [Fig. 7(c)], albeit broadened due to the worse energy resolution in this measurement.

3. Fitting analysis

Figures 7(e) and 7(f) show the fitting analysis results on the Ta $4f_{7/2}$ core-level spectra at 320 and 20 K, respectively.

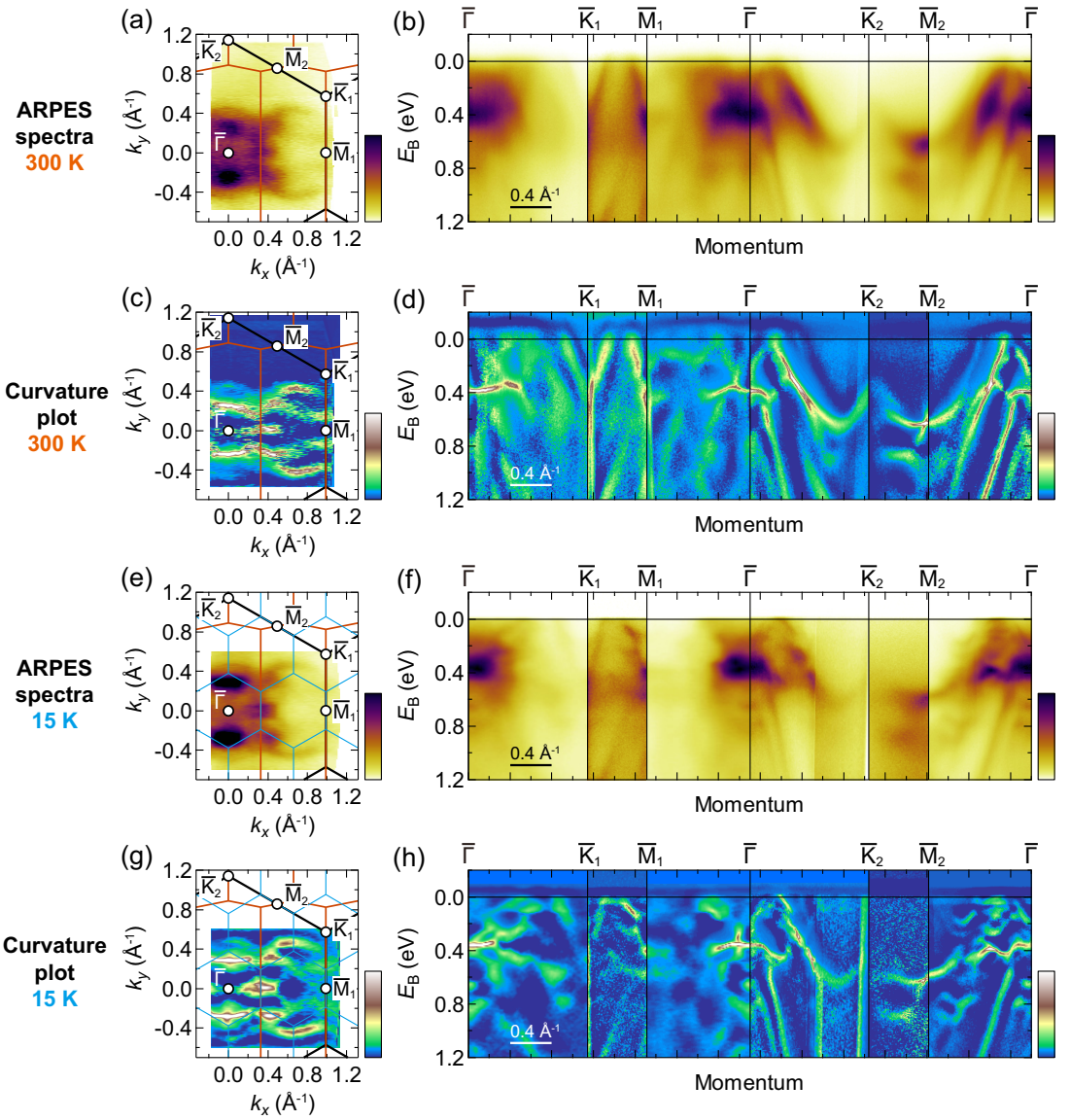

FIG. 9. Overview of ARPES intensity plots and their curvature plots. (a) ARPES intensity plots at E_F (integral width: 20 meV) collected at 300 K ($h\nu = 21.2$ eV). (b) ARPES spectra along $\bar{\Gamma}-\bar{K}_{1(2)}-\bar{M}_{1(2)}-\bar{\Gamma}$. (c), (d) The corresponding curvature plots (these are identical to Fig. 3 in the main text). (e)–(h) Same as (a)–(d), but at 15 K (LT phase).

The resulting parameters of Voigt functions are summarized in Table I. The number and relative intensity ratio of Voigt functions were set by considering the number of nonequivalent Ta sites [see Figs. 1(b) and 1(c) for the site notation]. Figure 7(g) depicts the fitting result of Te $4d_{5/2}$ at 320 K using three Voigt functions.

TABLE I. Fitting parameters of Voigt functions for the Ta $4f_{7/2}$ spectra.

	Ta site	E_B (eV)	Area ratio (fixed)	Gaussian FWHM (eV)	Lorentzian FWHM (eV)
320 K [Fig. 7(e)]	Ta1	22.68(1)	1	0.18	<0.01
	Ta2	22.78(3)	2	0.18	0.13
20 K [Fig. 7(f)]	Ta1A	22.51(1)	1	0.10	0.02
	Ta1B or Ta2B	22.62(4)	2	0.10	<0.01
		22.68(6)	2	0.10	0.02
	Ta2A	22.82(2)	4	0.10	0.12

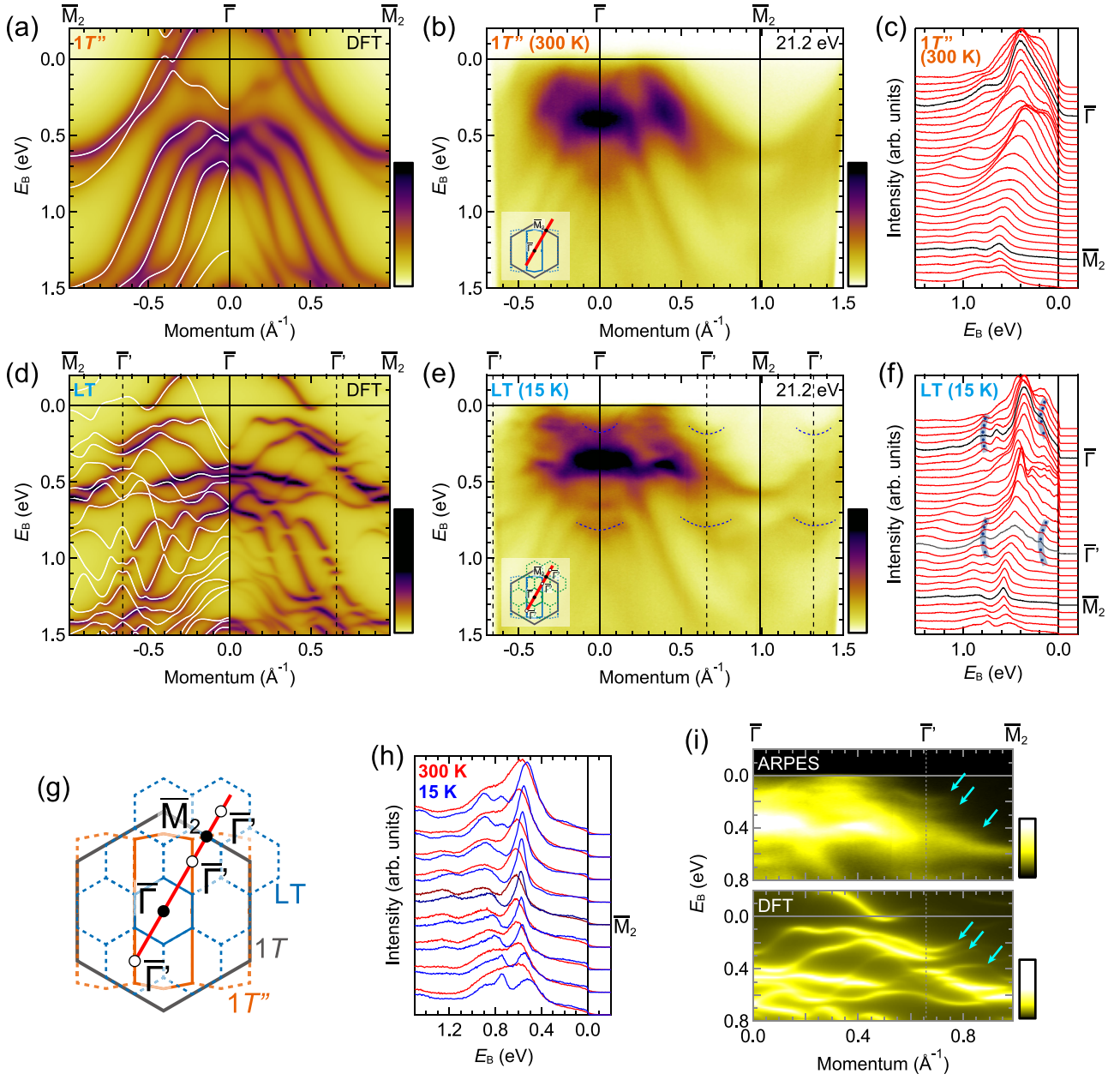

FIG. 10. Comparison of band structure along the $\bar{\Gamma}-\bar{M}_2$ direction between the $1T''$ and LT phases. (a)–(c) Band calculation (line dispersion and unfolding spectra) [(a)], ARPES spectra [(b)], and corresponding energy distribution curves [(c)] (integral width: 0.05 Å^{-1}) for the $1T''$ phase. ARPES data are collected with $h\nu = 21.2$ eV at 300 K. (d)–(f) Same as (a)–(c), but for the LT phase (ARPES data: 15 K). $\bar{\Gamma}'$ denotes the newly introduced Brillouin zone center. The broken blue lines in (e) and blue markers/shades in (f) highlight the characteristic dispersions centered at the $\bar{\Gamma}/\bar{\Gamma}'$ points. (g) Sketch of the (001) surface Brillouin zone. The red line shows the momentum cut of ARPES measurement. (h) Comparison of energy distribution curves at 300 K (red) and 15 K (blue). (i) Close-up comparison of ARPES spectra and band-unfolding spectra in the LT phase. The cyan arrows mark characteristic sharp submanifold structures.

APPENDIX C: TEMPERATURE DEPENDENCE OF VALENCE BAND POSITION

The temperature-dependent valence ARPES spectra were acquired simultaneously with the core-level spectra shown in Figs. 2 and 7. Figure 8(a) presents the Fermi surface image taken with synchrotron light ($h\nu = 90$ eV) at 320 K. The red arrow shows the momentum cut of the temperature-dependent ARPES measurements, which roughly aligns with the $\bar{\Gamma}-\bar{M}_2$ direction. Figure 8(b) displays the ARPES spectra taken at selected temperatures. At a momentum of ~0.9 Å^{-1} (the dashed blue box region), two characteristic band structures, which are identical to the flat bands appearing along $\bar{K}_1-\bar{M}_2-\bar{K}_2$, have their minima located at $E_B \sim 0.6$ and 0.9 eV. Since the dispersion of these flat bands is less modified through the $1T''$-LT phase transition (as elaborated in the main text), we can semiquantitatively evaluate the chemical potential shift by tracking the energy positions of these bands. Figure 8(c)

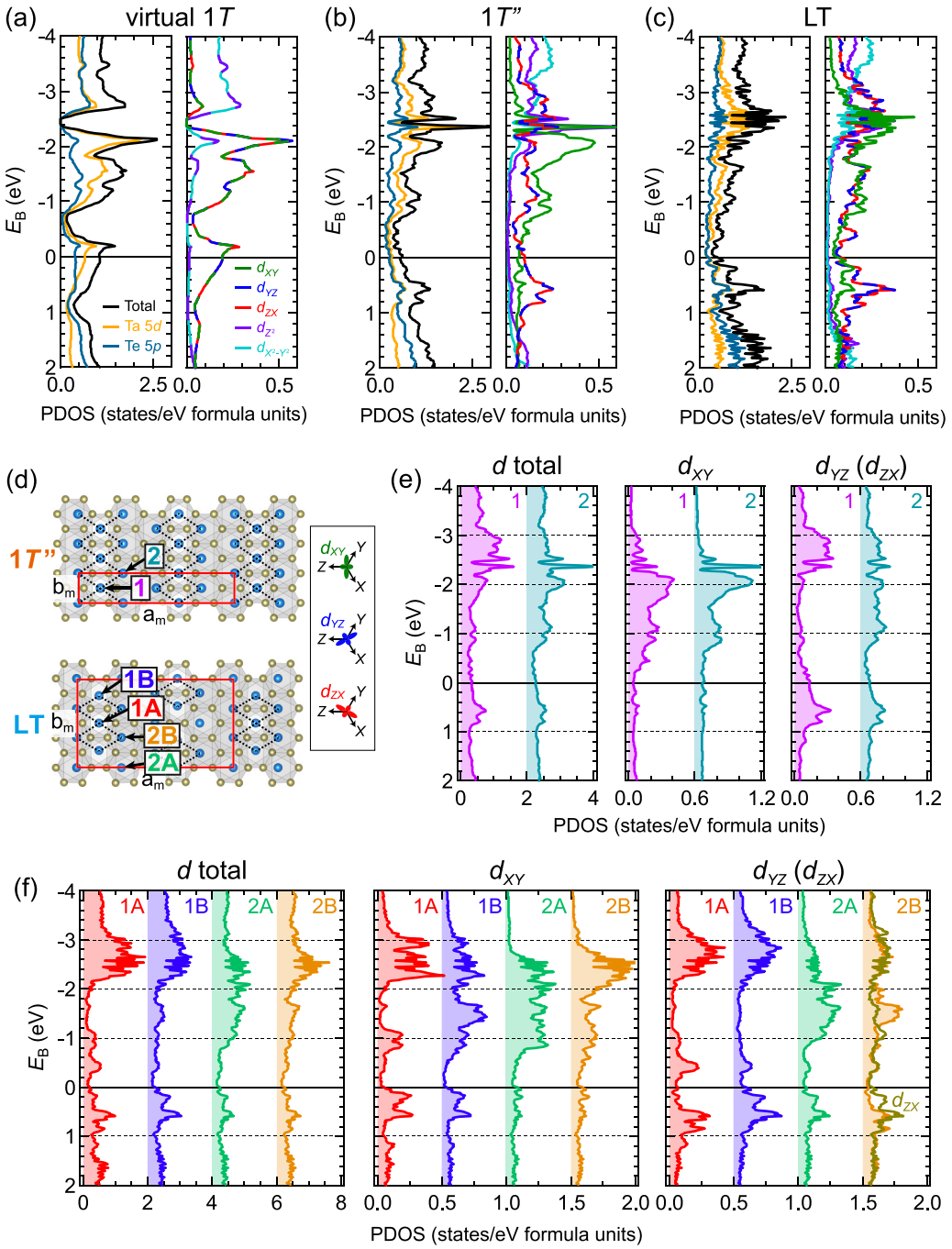

FIG. 11. Density of states calculations. (a)–(c) Orbital-resolved partial density of states (PDOS) for the virtual $1T$ [(a)], high-temperature $1T''$ [(b)], and LT phases [(c)]. The left panel shows the breakdown of total DOS [Ta $5d$ (orange) and Te $5p$ orbitals (cyan)], whereas the right panel indicates the breakdown of PDOS for Ta $5d$ ($d_{YZ}/d_{ZX}/d_{XY}/d_{Z^2}/d_{X^2-Y^2}$). (d) Notations of inequivalent Ta sites for the $1T''$ (1/2) and LT (1A/1B/2A/2B) phases. (e) Ta site-resolved PDOS for the d total, d_{XY} and d_{YZ} (d_{ZX}) in the $1T''$ phase. (f) Same as (e), but in the LT phase.

shows the energy distribution curves collected from 320 to 20 K in the dashed blue box region displayed in Fig. 8(b). The blue markers trace the peak positions of the shallower flat band, showing a downward shift from $E_B \sim 0.64$ to $\sim$0.59 eV upon cooling. The result is summarized in Fig. 8(d) with its uncertainty presented by error bars. The observed trend is well consistent with the temperature dependence of core-level spectral shifts shown in the main text [Fig. 2(g)].

APPENDIX D: RAW ARPES INTENSITY PLOTS ALONG HIGH-SYMMETRY LINES

Figures 9(a) and 9(b) show the ARPES intensity map at E_F (integral width: 20 meV) and the ARPES spectra along the $\bar{\Gamma}$–$\bar{K}_{1(2)}$–$\bar{M}_{1(2)}$–$\bar{\Gamma}$ direction recorded at 300 K ($1T''$ phase) with a He-discharge lamp ($h\nu = 21.2$ eV). The curvature plots [Figs. 9(c) and 9(d), which are identical to Figs. 3(c) and 3(d)]

are obtained from these raw data. Figures 9(c)–9(h) present the data at 15 K (LT phase).

APPENDIX E: SIGNATURE OF (3 × 3)-FOLDING BAND STRUCTURE IN THE LT PHASE

Figures 10(a)–10(c) respectively show the band calculation, ARPES spectra ($h\nu = 21.2$ eV, 300 K), and corresponding energy distribution curves along the $\bar{\Gamma}-\bar{M}_2$ direction for the high-temperature $1T''$ phase. Figures 10(d)–10(f) present the dataset for the LT phase (ARPES data collected at 15 K). Here, $\bar{\Gamma}'$ denotes the newly introduced Brillouin zone center resulting from the (3 × 3) superstructure formation in the LT phase, as schematically depicted in Fig. 10(g). As discussed in the main text, significant spectral reconstructions occur through the $1T''$-LT phase transition. Specifically, we can also track the distinct downward convex dispersions centered at both $\bar{\Gamma}$ and $\bar{\Gamma}'$ points, as highlighted by the broken blue lines in Fig. 10(e) and the blue markers/shades in Fig. 10(f). These characteristic replica bands are not found in the $1T''$ data and thus indicate the signature of the band-folding effect.

In Fig. 10(h), we compare the energy distribution curves around $\bar{M}_2$ at 300 K (red) and 15 K (blue). This comparison clearly demonstrates that the overall band dispersions shift to a lower E_B region upon cooling, consistent with the data presented in Appendix C (Fig. 8). In addition, we observe weak but discernible peak structures near the Fermi level ($E_B < 0.4$ eV) appearing at 15 K. Figure 10(i) shows a close-up comparison between the ARPES image and the band-unfolding spectra for the LT phase with a different color scale. The observed sharp submanifold structures, indicated by the arrows, are faithfully reproduced by the calculation.

APPENDIX F: DETAILS OF ORBITAL-RESOLVED BAND CALCULATIONS

Figures 11(a)–11(c) show the orbital-resolved PDOS for the virtual $1T$, high-temperature $1T''$, and LT phases, respectively. As displayed in the left panels, comparable states of Ta $5d$ and Te $5p$ orbitals reside in the vicinity of the Fermi level for all three phases. The right panels present the breakdown of total DOS for the five Ta $5d$ orbitals. The PDOS near the Fermi level are mainly derived from t_{2g} orbitals, namely, the $d_{XY}/d_{YZ}/d_{ZX}$ states. The PDOS for $1T''$ and LT phases can be further decomposed into the contributions from inequivalent Ta sites [see Fig. 11(d)]. Figures 11(e) and 11(f) provide a summary of the atomic/orbital-resolved PDOS distributions for the $1T''$ and LT phases, respectively. We note that the PDOS distributions for d_{YZ} and d_{ZX} are equivalent due to the $C2/m$ symmetry for all Ta sites, except for the Ta2B sites in LT.

Figure 12 displays the orbital-resolved band calculations along $\bar{K}_1-\bar{M}_1-\bar{K}_1$ and $\bar{K}_1-\bar{M}_2-\bar{K}_2$, presented by separated panels for each orbital. Figures 5(e) and 5(h) are constructed from these data.

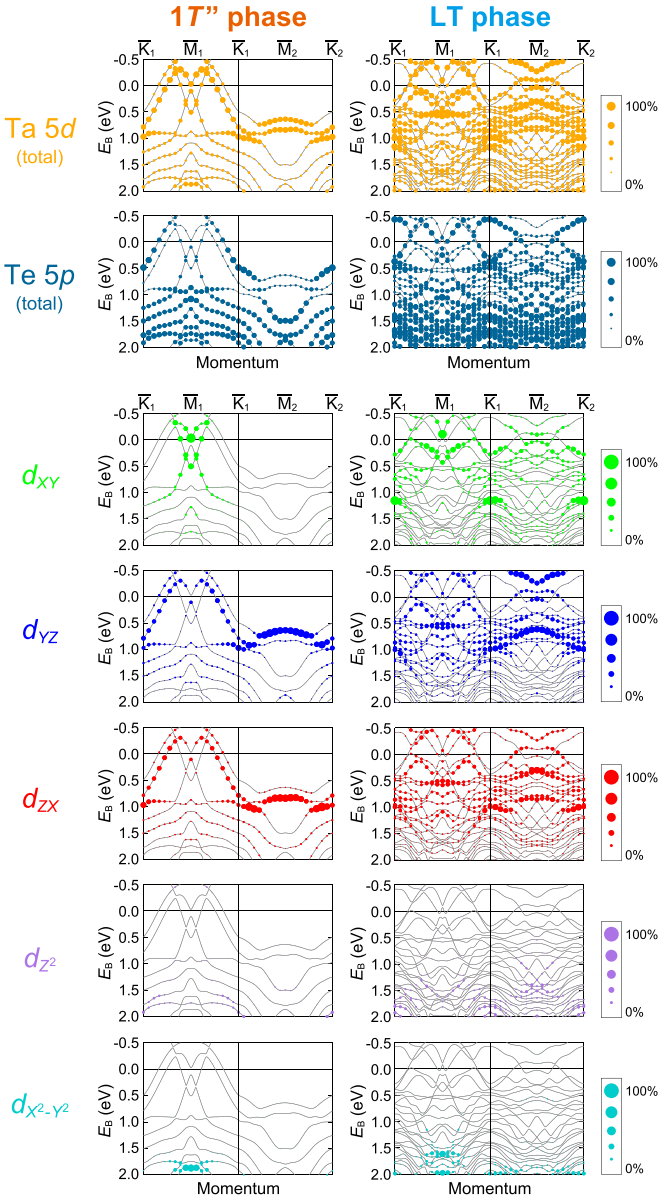

FIG. 12. Orbital-projected band calculations along $\bar{K}_1-\bar{M}_1-\bar{K}_1$ and $\bar{K}_1-\bar{M}_2-\bar{K}_2$ for each orbital (Ta $5d$ total, Te $5p$ total, and five Ta $5d$ orbitals).

APPENDIX G: FAINT LT-PHASE BAND FEATURES OBSERVED UP TO ROOM TEMPERATURE

Figure 13(a) shows the enlarged ARPES image along $\bar{K}_1-\bar{M}_1-\bar{K}_1$ measured at 300 K ($h\nu = 21.2$ eV). As can be seen from the peak plots of its momentum distribution curves, the spectral intensity of the V-shaped band (centered at $\bar{M}_1$) already exhibits a slight kink-like feature (see also the white arrows). Such kink-like feature is not found in the calculation for the $1T''$ phase [Fig. 13(f)] but is rather unique to the LT phase [Fig. 13(h)]. This is also the case for the dispersiveless bands located at $E_B \sim 0.5$ eV; Figs. 13(b)–13(i) compare the band structures and their typical energy distribution curves for the ARPES data [300 K (b), (c) and 15 K (d), (e)] and band calculations [$1T''$ phase (f), (g) and LT phase (h), (i)]. While the dispersiveless band structures are characteristic of the LT

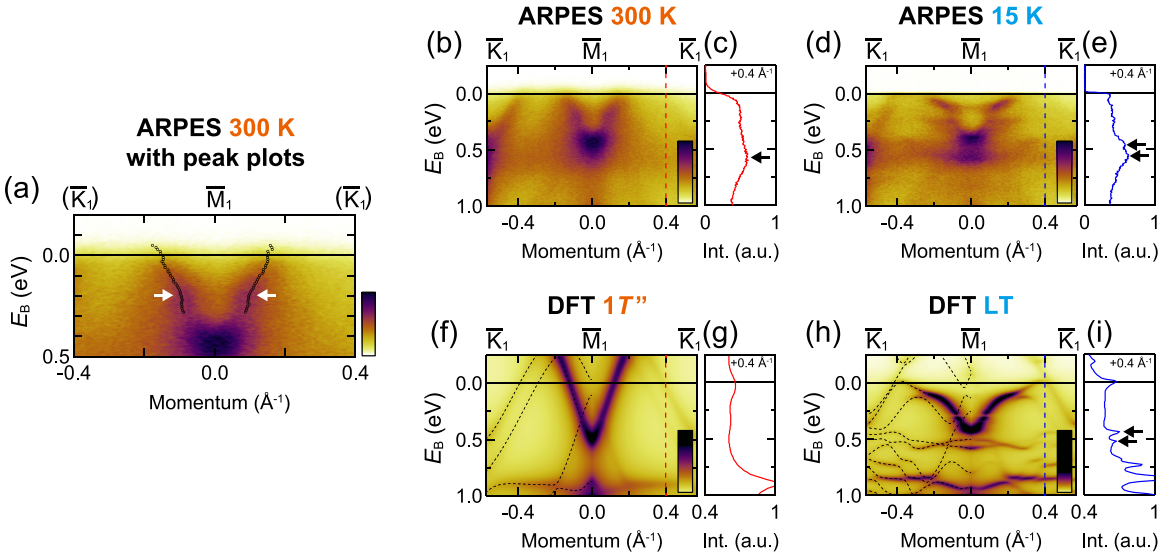

FIG. 13. Signatures of the LT-phase features observed up to room temperature. (a) Enlarged ARPES image at 300 K along $\bar{K}_1-\bar{M}_1-\bar{K}_1$. The markers indicate the peak positions of the momentum distribution curves, which trace the faint kink-like feature (see also the white arrows). (b)–(e) ARPES spectra and energy distribution curve at a momentum of $+0.4$ Å^{-1} (integral width: 0.05 Å^{-1}) collected at 300 K [(b), (c)] and 15 K [(d), (e)]. The black arrows mark the spectral peak assigned to the less-dispersive band structures lying at $E_B \sim 0.5$ eV. (f)–(i) Corresponding band (unfolding) calculation for the $1T''$ [(f), (g)] and LT [(h), (i)] phases. All spectral data in this figure are identical to those shown in Fig. 5.

phase [see also the black arrows in Figs. 13(e) and 13(i)], their spectral weights are vaguely seen at 300 K [Fig. 13(c)]. These LT-like signatures observed up to room temperature probably reflect the inherent structural fluctuation hosting in $TaTe_2$.

[1] J. A. Wilson and A. D. Yoffe, The transition metal dichalcogenides discussion and interpretation of the observed optical, electrical and structural properties, Adv. Phys. **18**, 193 (1969).

[2] M. Chhowalla, H. S. Shin, G. Eda, L.-J. Li, K. P. Loh, and H. Zhang, The chemistry of two-dimensional layered transition metal dichalcogenide nanosheets, Nat. Chem. **5**, 263 (2013).

[3] G. Grüner, *Density Waves in Solids* (Addison-Wesley, Reading, MA, 1994).

[4] M. D. Johannes and I. I. Mazin, Fermi surface nesting and the origin of charge density waves in metals, Phys. Rev. B **77**, 165135 (2008).

[5] X. Zhu, Y. Cao, J. Zhang, E. W. Plummer, and J. Guo, Classification of charge density waves based on their nature, Proc. Natl. Acad. Sci. USA **112**, 2367 (2015).

[6] B. Sipos, A. F. Kusmartseva, A. Akrap, H. Berger, L. Forró, and E. Tutiš, From Mott state to superconductivity in 1T-TaS_2, Nat. Mater. **7**, 960 (2008).

[7] M. Leroux, I. Errea, M. Le Tacon, S.-M. Souliou, G. Garbarino, L. Cario, A. Bosak, F. Mauri, M. Calandra, and P. Rodière, Strong anharmonicity induces quantum melting of charge density wave in 2*H*-$NbSe_2$ under pressure, Phys. Rev. B **92**, 140303(R) (2015).

[8] M. H. Whangbo and E. Canadell, Analogies between the concepts of molecular chemistry and solid-state physics concerning structural instabilities. Electronic origin of the structural modulations in layered transition metal dichalcogenides, J. Am. Chem. Soc. **114**, 9587 (1992).

[9] E. Canadell, S. Jobic, R. Brec, J. Rouxel, and M.-H. Whangbo, Importance of short interlayer Te···Te contacts for the structural distortions and physical properties of CdI_2-type layered transition-metal ditellurides, J. Solid State Chem. **99**, 189 (1992).

[10] A. Vernes, H. Ebert, W. Bensch, W. Heid, and C. Näther, Crystal structure, electrical properties and electronic band structure of tantalum ditelluride, J. Phys.: Condens. Matter **10**, 761 (1998).

[11] M.-L. Doublet, S. Remy, and F. Lemoigno, Density functional theory analysis of the local chemical bonds in the periodic tantalum dichalcogenides TaX_2 (X = S, Se, Te), J. Chem. Phys. **113**, 5879 (2000).

[12] D. C. Miller, S. D. Mahanti, and P. M. Duxbury, Charge density wave states in tantalum dichalcogenides, Phys. Rev. B **97**, 045133 (2018).

[13] B. E. Brown, The crystal structures of WTe_2 and high-temperature $MoTe_2$, Acta Crystallogr. **20**, 268 (1966).

[14] G. L. Pascut, K. Haule, M. J. Gutmann, S. A. Barnett, A. Bombardi, S. Artyukhin, T. Birol, D. Vanderbilt, J. J. Yang, S.-W. Cheong, and V. Kiryukhin, Dimerization-induced cross-layer quasi-two-dimensionality in metallic $IrTe_2$, Phys. Rev. Lett. **112**, 086402 (2014).

[15] G. Tunell and L. Pauling, The atomic arrangement and bonds of the gold-silver ditellurides, Acta Crystallogr. **5**, 375 (1952).

[16] K. D. Bronsema, G. W. Bus, and G. A. Wiegers, The crystal structure of vanadium ditelluride, $V_{1+x}Te_2$, J. Solid State Chem. **53**, 415 (1984).

[17] B. E. Brown, The crystal structures of $NbTe_2$ and $TaTe_2$, Acta Crystallogr. **20**, 264 (1966).

[18] N. Mitsuishi, Y. Sugita, M. S. Bahramy, M. Kamitani, T. Sonobe, M. Sakano, T. Shimojima, H. Takahashi, H. Sakai, K. Horiba, H. Kumigashira, K. Taguchi, K. Miyamoto, T. Okuda, S. Ishiwata, Y. Motome, and K. Ishizaka, Switching of band inversion and topological surface states by charge density wave, Nat. Commun. **11**, 2466 (2020).

[19] A. Nakamura, T. Shimojima, M. Matsuura, Y. Chiashi, M. Kamitani, H. Sakai, S. Ishiwata, H. Li, A. Oshiyama, and K. Ishizaka, Evaluation of photo-induced shear strain in monoclinic VTe_2 by ultrafast electron diffraction, Appl. Phys. Express **11**, 092601 (2018).

[20] A. Nakamura, T. Shimojima, Y. Chiashi, M. Kamitani, H. Sakai, S. Ishiwata, H. Li, and K. Ishizaka, Nanoscale imaging of unusual photoacoustic waves in thin flake VTe_2, Nano Lett. **20**, 4932 (2020).

[21] T. Sörgel, J. Nuss, U. Wedig, R. K. Kremer, and M. Jansen, A new low temperature modification of $TaTe_2$—Comparison to the room temperature and the hypothetical 1T-$TaTe_2$ modification, Mater. Res. Bull. **41**, 987 (2006).

[22] T. Ohtani, K. Hayashi, M. Nakahira, and H. Nozaki, Phase transition in $V_{1+x}Te_2$ ($0.04 \leqslant x \leqslant 0.11$), Solid State Commun. **40**, 629 (1981).

[23] I. E. Baggari, N. Sivadas, G. M. Stiehl, J. Waelder, D. C. Ralph, C. J. Fennie, and L. F. Kourkoutis, Direct visualization of trimerized states in $1T'$—$TaTe_2$, Phys. Rev. Lett. **125**, 165302 (2020).

[24] Y. Liu, W. J. Lu, D. F. Shao, L. Zu, X. C. Kan, W. H. Song, and Y. P. Sun, Structural, electrical, and thermoelectric properties of distorted 1T—$Ta_{1-x}Nb_xTe_2$ single crystals, Europhys. Lett. **109**, 17003 (2015).

[25] H. Luo, W. Xie, J. Tao, H. Inoue, A. Gyenis, J. W. Krizan, A. Yazdani, Y. Zhu, and R. J. Cava, Polytypism, polymorphism, and superconductivity in $TaSe_{2-x}Te_x$, Proc. Natl. Acad. Sci. USA **112**, E1174 (2015).

[26] Y. Liu, D. F. Shao, L. J. Li, W. J. Lu, X. D. Zhu, P. Tong, R. C. Xiao, L. S. Ling, C. Y. Xi, L. Pi, H. F. Tian, H. X. Yang, J. Q. Li, W. H. Song, X. B. Zhu, and Y. P. Sun, Nature of charge density waves and superconductivity in $1T$—$TaSe_{2-x}Te_x$, Phys. Rev. B **94**, 045131 (2016).

[27] Y.-C. Luo, Y.-Y. Lv, R.-M. Zhang, L. Xu, Z.-A. Zhu, S.-H. Yao, J. Zhou, X.-X. Xi, Y. B. Chen, and Y.-F. Chen, Subtle effect of doping on the charge density wave in $TaTe_{2-\delta}$(δ = 0.028—0.123) crystals revealed by anisotropic transport measurements and Raman spectroscopy, Phys. Rev. B **103**, 064103 (2021).

[28] J. Guo, C. Huang, H. Luo, H. Yang, L. Wei, S. Cai, Y. Zhou, H. Zhao, X. Li, Y. Li, K. Yang, A. Li, P. Sun, J. Li, Q. Wu, R. J. Cava, and L. Sun, Observation of three superconducting transitions in the pressurized CDW-bearing compound $TaTe_2$, Phys. Rev. Mater. **6**, L051801 (2022).

[29] K. M. Siddiqui, D. B. Durham, F. Cropp, C. Ophus, S. Rajpurohit, Y. Zhu, J. D. Carlström, C. Stavrakas, Z. Mao, A. Raja, P. Musumeci, L. Z. Tan, A. M. Minor, D. Filippetto, and R. A. Kaindl, Ultrafast optical melting of trimer superstructure in layered 1T′-$TaTe_2$, Commun. Phys. **4**, 152 (2021).

[30] J. Hwang, Y. Jin, C. Zhang, T. Zhu, K. Kim, Y. Zhong, J.-E. Lee, Z. Shen, Y. Chen, W. Ruan, H. Ryu, C. Hwang, J. Lee, M. F. Crommie, S.-K. Mo, and Z.-X. Shen, A novel $\sqrt{19} \times \sqrt{19}$ superstructure in epitaxially grown 1T-$TaTe_2$, Adv. Mater. **34**, 2204579 (2022).

[31] I. Di Bernardo, J. Ripoll-Sau, J. A. Silva-Guillén, F. Calleja, C. G. Ayani, R. Miranda, E. Canadell, M. Garnica, and A. L. Vázquez de Parga, Metastable polymorphic phases in monolayer $TaTe_2$, Small **19**, 2300262 (2023).

[32] Y. Lin, M. Huber, S. Rajpurohit, Y. Zhu, K. M. Siddiqui, D. H. Eilbott, L. Moreschini, P. Ai, J. D. Denlinger, Z. Mao, L. Z. Tan, and A. Lanzara, Evidence of nested quasi-one-dimensional Fermi surface and decoupled charge-lattice orders in layered $TaTe_2$, Phys. Rev. Res. **4**, L022009 (2022).

[33] J. Feng, A. Tan, S. Wagner, J. Liu, and Z. Mao, X. Ke, and P. Zhang, Charge modulation and structural transformation in $TaTe_2$ studied by scanning tunneling microscopy/spectroscopy, Appl. Phys. Lett. **109**, 021901 (2016).

[34] J. J. Gao, J. G. Si, X. Luo, J. Yan, F. C. Chen, G. T. Lin, L. Hu, R. R. Zhang, P. Tong, W. H. Song, X. B. Zhu, W. J. Lu, and Y. P. Sun, Origin of the structural phase transition in single-crystal $TaTe_2$, Phys. Rev. B **98**, 224104 (2018).

[35] C. Chen, H.-S. Kim, A. S. Admasu, S.-W. Cheong, K. Haule, D. Vanderbilt, and W. Wu, Trimer bonding states on the surface of the transition-metal dichalcogenide $TaTe_2$, Phys. Rev. B **98**, 195423 (2018).

[36] V. Petkov, K. Chapagain, J. Yang, S. Shastri, and Y. Ren, Exotic bonding interactions and coexistence of chemically distinct periodic lattice distortions in the charge density wave compound $TaTe_2$, Phys. Rev. B **102**, 024111 (2020).

[37] See http://www.openmx-square.org/.

[38] J. P. Perdew and Alex Zunger, Self-interaction correction to density-functional approximations for many-electron systems, Phys. Rev. B **23**, 5048 (1981).

[39] J. P. Perdew, K. Burke, and M. Ernzerhof, Generalized gradient approximation made simple, Phys. Rev. Lett. **77**, 3865 (1996).

[40] W. Ku, T. Berlijn, and C.-C. Lee, Unfolding first-principles band structures, Phys. Rev. Lett. **104**, 216401 (2010).

[41] C.-C. Lee, Y. Yamada-Takamura, and T. Ozaki, Unfolding method for the first-principles LCAO electronic structure calculations, J. Phys.: Condens. Matter **25**, 345501 (2013).

[42] H. P. Hughes and J. A. Scarfe, Site specific photohole screening in a charge density wave, Phys. Rev. Lett. **74**, 3069 (1995).

[43] K. Horiba, K. Ono, J. H. Oh, T. Kihara, S. Nakazono, M. Oshima, O. Shiino, H. W. Yeom, A. Kakizaki, and Y. Aiura, Charge-density wave and three-dimensional Fermi surface in $1T$-$TaSe_2$ studied by photoemission spectroscopy, Phys. Rev. B **66**, 073106 (2002).

[44] K. Rossnagel, On the origin of charge-density waves in select layered transition-metal dichalcogenides, J. Phys.: Condens. Matter **23**, 213001 (2011).

[45] Y. Fei, Z. Wu, W. Zhang, and Y. Yin, Understanding the Mott insulating state in $1T$-TaS_2 and $1T$-$TaSe_2$, AAPPS Bull. **32**, 20 (2022).

[46] T. Qian, H. Miao, Z. J. Wang, X. Shi, Y. B. Huang, P. Zhang, N. Xu, L. K. Zeng, J. Z. Ma, P. Richard, M. Shi, G. Xu, X. Dai, Z. Fang, A. F. Fang, N. L. Wang, and H. Ding, Structural phase transition associated with van Hove singularity in 5D transition metal compound $IrTe_2$, New J. Phys. **16**, 123038 (2014).

[47] P. Zhang, P. Richard, T. Qian, Y.-M. Xu, X. Dai, and H. Ding, A precise method for visualizing dispersive features in image plots, Rev. Sci. Instrum. **82**, 043712 (2011).

[48] C. Battaglia, H. Cercellier, F. Clerc, L. Despont, M. G. Garnier, C. Koitzsch, P. Aebi, H. Berger, L. Forró, and C. Ambrosch-Draxl, Fermi-surface-induced lattice distortion in $NbTe_2$, Phys. Rev. B **72**, 195114 (2005).

[49] I. Kar, K. Dolui, L. Harnagea, Y. Kushnirenko, G. Shipunov, N. C. Plumb, M. Shi, B. Büchner, and S. Thirupathaiah, Experimental evidence of a stable $2H$ phase on the surface of layered $1T'-TaTe_2$, J. Phys. Chem. C **125**, 1150 (2021).

[50] T. C. Hu, Q. Wu, Z. X. Wang, L. Y. Shi, Q. M. Liu, L. Yue, S. J. Zhang, R. S. Li, X. Y. Zhou, S. X. Xu, D. Wu, T. Dong, and N. L. Wang, Optical spectroscopy and ultrafast pump-probe study of the structural phase transition in $1T'-TaTe_2$, Phys. Rev. B **105**, 075113 (2022).

[51] M.-H. Whangbo, E. Canadell, P. Foury, and J.-P. Pouget, Hidden Fermi surface nesting and charge density wave instability in low-dimensional metals, Science **252**, 96 (1991).

[52] K. Kim, S. Kim, K.-T. Ko, H. Lee, J.-H. Park, J. J. Yang, S.-W. Cheong, and B. I. Min, Origin of first-order-type electronic and structural transitions in $IrTe_2$, Phys. Rev. Lett. **114**, 136401 (2015).

[53] N. Katayama, S. Tamura, T. Yamaguchi, K. Sugimoto, K. Iida, T. Matsukawa, A. Hoshikawa, T. Ishigaki, S. Kobayashi, Y. Ohta, and H. Sawa, Large entropy change derived from orbitally assisted three-centered two-electron σ bond formation in metallic $Li_{0.33}VS_2$, Phys. Rev. B **98**, 081104(R) (2018).

[54] N. Katayama, Y. Matsuda, K. Kojima, T. Hara, S. Kitou, N. Mitsuishi, H. Takahashi, S. Ishiwata, K. Ishizaka, and H. Sawa, Observation of local atomic displacements intrinsic to the double zigzag chain structure of $1T$-MTe_2 (M = V, Nb, Ta), Phys. Rev. B **107**, 245113 (2023).

[55] H. Chen, Z. Li, L. Guo, and X. Chen, Anisotropic magnetotransport and magnetic properties of low-temperature phase of $TaTe_2$, Europhys. Lett. **117**, 27009 (2017).

[56] K. Momma and F. Izumi, *VESTA 3* for three-dimensional visualization of crystal, volumetric and morphology data, J. Appl. Crystallogr. **44**, 1272 (2011).